Quantum Dipole Effects in a Silicon Transistor under High Electric Fields

Shinichi Saito[1*], Zuo Li[1], Hiroyuki Yoshimoto[2], Isao Tomita[1,3], Yoshishige Tsuchiya[4], Yoshitaka Sasago[5], Hideo Arimoto[1,5], Fayong Liu[1], Muhammad Khaled Husain[1], Digh Hisamoto[5], Harvey N. Rutt[1], & Susumu Kurihara[2]

[1]*Sustainable Electronic Technologies, Electronics and Computer Science, Faculty of Physical Sciences and Engineering, University of Southampton, SO17 1BJ, UK*

[2]*Department of Physics, Waseda University, Shinjuku, Tokyo 169-8555, Japan*

[3]*Department of Electrical and Computer Engineering, National Institute of Technology, Gifu College, 2236-2 Kamimakuwa, Motosu, Gifu 501-0495, Japan*

[4]*Smart Electronic Materials and Systems, Electronics and Computer Science, Faculty of Physical Sciences and Engineering, University of Southampton, SO17 1BJ, UK*

[5]*Research & Development Group, Hitachi, Ltd., 1-280 Higashikoigakubo, Kokubunji, Tokyo 185-8601, Japan*

Strongly correlated one-dimensional systems are paradigms for theoretical condensed-matter physics, since various predictions such as spin-charge separation and topological phase transitions can be determined based on mathematically rigid models. Some of these features were experimentally observed in carbon nanotubes and chiral edge states of quantum Hall systems. Here, we show the emergence of another one-dimensional system in a nanoscale silicon field-effect-transistor with a wide and short hole channel when a strong electric field is applied at low temperatures. We observed the quantum dipoles, which form at the ultra-thin gate interface and exhibit a phase transition, and the drain current showed a clear, negative differential conductance due to the screening of electric fields by antiferroelectric ordering. We have also found new current plateaus against drain voltages, which corresponds to the magnetisation plateau theoretically predicted by the one-dimensional spin model. We obtained phase diagrams of the field-induced phase transitions by gate-induced doping.

*s.saito@soton.ac.uk

1. Introduction

Strongly correlated electron systems[1,2] exhibit a variety of exotic phenomena such as fractional quantum Hall effects,[3] Bose-Einstein condensation (BEC)[4,5] of excitons, high critical temperature (T_c) superconductivity,[6] Mott transitions,[6] magnetism,[7] quantum phase transitions,[8] and topological phase transitions.[2,7] In general, it is quite difficult to solve quantum many-body problems, because of the infinite degrees of freedom under the quantum mechanical superposition principle.[1,2] Classical computers using silicon (Si) complementary metal-oxide-semiconductor (CMOS) field-effect-transistors (FETs)[9] are not sufficient enough to completely solve these problems, and quantum simulators[10,11] will be powerful tools for analysing these systems in the future. Quantum simulators have also been proposed for elucidating the early universe using lattice gauge theories and quantum electrodynamics.[12]

The essential element and, thus, the grand challenge in fabricating a quantum simulator is the preparation of a *pseudo spin* (namely, a quantum bit, which is known as a qubit), which can point within the plane perpendicular to the (*pseudo*) magnetic field to allow the superposition state.[10,11] Many architectures can be used to generate the pseudo-spin, and significant progress has been achieved both theoretically and experimentally in systems using superconducting circuitries,[13,14] ultracold atoms,[15] exciton-polariton condensates,[5] integrated photonic waveguides,[16] photonic crystals,[17] and entangled photons.[18] Most of these technologies[13–15] are based on low temperature operations, and even photonic systems[16–18] will require superconducting single-photon detectors operating at low temperatures.[19] As the integration density of qubits[20,21] increases over time, CMOS circuitries operating at low temperatures will be required to facilitate error-tolerant operations of quantum simulators.[20,21] To ensure the reliability of the circuitries, we must make sure to understand the transport mechanisms in nanoscale CMOSFETs at low temperatures. The advantages of using Si technologies[9] for quantum applications[20,22] include their tremendous integration capabilities in addition to the state-of-the-art fabrication infrastructures, which will be available throughout the world for mass production.

Si CMOSFETs using two-dimensional (2*D*) electron and hole gas systems[23] are fundamental building blocks in modern digital computing for information and communications technologies (ICT) based on the Boolean logic.[9,24] In recent years, booster technologies such as high-κ/metal-gate stacks,[25] strained-Si,[26] and FinFETs[27] were successfully introduced to continue the scaling of Moore's law.[24] Now, Si technologies are among the most

advanced nanotechnologies, which means the world envisioned by Feynman[28] sixty years ago has come to fruition. An *n*-channel Si MOSFET was also used to identify the plateaus in Hall conductance under the application of strong magnetic fields at low temperature.[23,29–31] Moreover, single electron spin[20,22] and an elementary charge state[32,33] in Si are also candidates for generating qubits.[20,34]

Motivated by a possible future application in a CMOS circuit for a quantum simulator in the future, we evaluated a scaled Si MOSFET at low temperatures. To our surprise, we have found unusual anomalous transport properties in a wide and short-channel *p*-MOSFET when a *high transverse electric field* is applied. This means that we have made a one-dimensional ($1D$) hole channel. In addition, we examined the transport perpendicular to the $1D$ system. $1D$ systems are ideal for investigating strongly correlated electron systems, since various theoretical methods are available, including bosonisation,[35,36] Bethe ansatz,[37] and the renormalisation group.[38] Therefore, reliable predictions are available,[39–48] regardless of the absence of long-range order due to large quantum and thermal fluctuations.[49] Experimentally, $1D$ Tomonaga-Luttinger liquid (TLL) properties, which are characterised by the spin-charge separation, were found in carbon nanotubes,[50,51] chiral edge states,[52] GaAs quantum wires,[53,54] and Si nanowires.[55] In these previous experiments, the transport properties were examined in the *longitudinal* direction along the $1D$ system under weak electric fields to observe the nonlinear transport properties.[50–55]

Here we show *quantum dipoles* at the gate interface are responsible for the observed field-induced phase transition from thermally excited classical transport to quantum transport in the nano-scale Si transistor. An electric dipole is the dual of a magnetic spin, since Einstein's special theory of relativity ensures the equivalence of electricity and magnetism under Lorentz transformation.[56] In reality, this duality is broken in many cases due to the absence of magnetic monopoles[57] at least in the low energy scale important for condensed-matter physics, where material properties are dominated by electrons. Therefore, various quantum spin states such as ferro- and Anti-Ferro(AF)-magnets are known in strongly correlated magnetic systems,[7,42,52,58] while electric counterparts using quantum dipoles are missing[59] due to the lack of an elementary particle with the internal dipole freedom. Regardless of the limited number of elementary particles, however, various exotic excitations have been emerged in solid states, e.g., Cooper pairs in superconductors,[6,60,61] fractional charged composite quasi-particles in quantum Hall systems,[3,23,29,30,62,63] massless Dirac fermions in graphene,[64] vortex-anti-vortex pairs in topological phase transitions of Berezinskii-Kosterlitz-Thouless (BKT),[65–67] to name a few. The idea of this work is to make a quantum dipole as a composite bound

state of an electron-hole pair. We show the interactions between dipoles were described by a quantum dipole model equivalent to a 1D spin-half model. This reveals the emergence of a new, 1D, strongly correlated, many-body system using Si, in which the carrier concentrations and electric fields are highly and reliably tunable. We found a new current plateau by gate-induced doping in the transistor, and the plateau will be correlated with a magnetisation plateau theoretically predicted in a spin system.[44–47)]

2. Experimental Details

2.1 Anomalous transport in 1D channel at the edge

We used a *p*-channel (a channel for holes, which are *positive* charged carriers) MOSFET with a gate length (L, all abbreviations and variables are summarised in Table A-1) of 55 nm and a width (W) of 10 μm, which has a high aspect ratio of (approximately 180, Figs. 1 (a) - 1 (c)). We chose a device with a wide channel to form a 1D channel along the gate (Fig. 1 (c)), and a short channel was used to apply a high transverse electric field. By applying the larger drain voltages to the channel, we could push the channel further away from the drain edge due to the smaller voltage difference between the gate and the drain voltages. As a result, the channel is confined at the source edge due to the higher electric field from the gate to the source electrodes, which are separated by the extremely thin silicon-oxynitride (SiON) layer with an equivalent oxide thickness (EOT, t_{ox}) of 2.4 nm (Fig. 1 (b)). This is the so called *pinch-off* of the channel,[9)] and holes are accumulated along the source edge. The 2D quantum mechanical confinements in long-channel CMOS are observed even at room temperature,[9,23)] and if L is sufficiently small we expect another confinement in 1D after the pinch-off of the channel. Our system is unique in that the higher the transverse electric field, the stronger the 1D confinement. Therefore, we expected to observe 1D properties under the higher transverse electric fields, while the weak longitudinal electric fields are usually used to probe the nonlinear transport properties.[50–54)] These inverted holes are injected into the pinch-off region as highly energetic hot holes, which allows us to use I_d as a probe to examine the electronic state of the 1D channel. Therefore, partners (holes) of electrons, which form the dipole pairs (excitons), are continuously changing even though the average dipole moments remain finite at the source edge in the saturation region. The transistor's typical drain current (I_d) dependence of the transistor on the gate voltage (V_g) is shown in Fig. 1 (d). We found a remarkable kink at 5 K, but such an anomaly was not observed at 298 K.

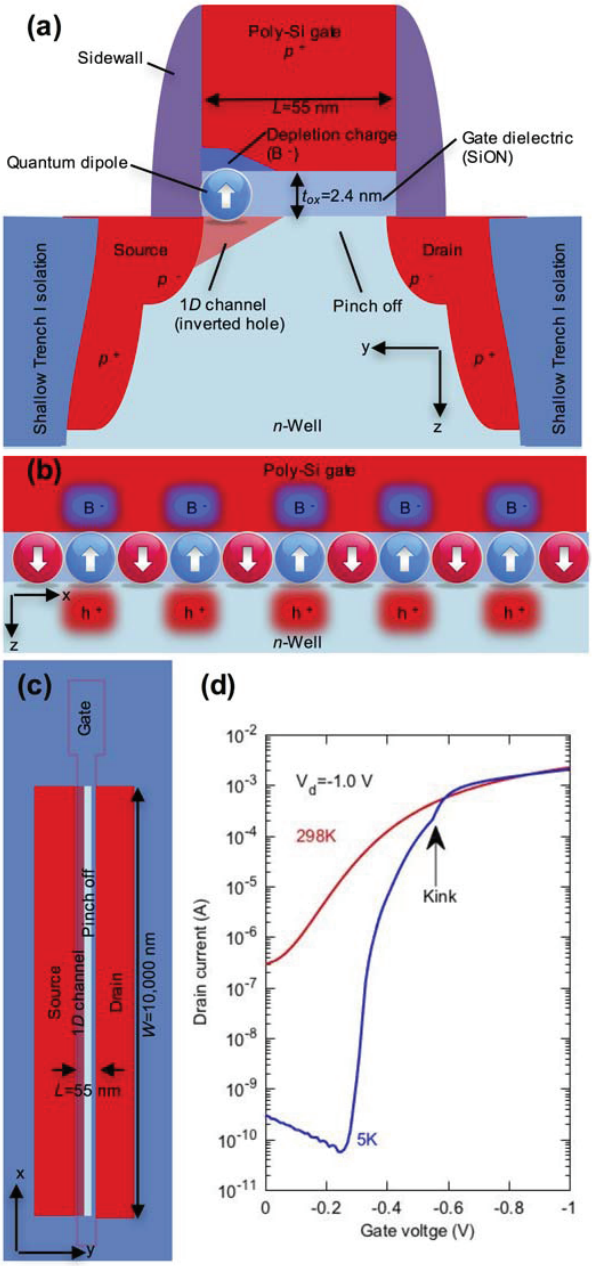

Fig. 1. (Color) 1D channel formation in a Si p-MOSFET. (a) A cross sectional image. After the pinch-off, the inverted holes are accumulated at the source edge. (b) A cross sectional image of the device at the gate stack. Dipoles generated by the depletion charges and channel holes are formed at the interface due to the high electric fields. (c) A plane-view image of the device. (d) Typical $I_{\rm d} - V_{\rm g}$ curves at 5 K and 298 K.

2.2 Negligible impact of local heating

First, we confirmed that the kink did not originate from the local heating (Figs. 2 and 3). We used a cryogen-free low-temperature measurement system (Cryogenic limited), which uses the expansion of the compressed helium gas for cooling. The variable temperature insert

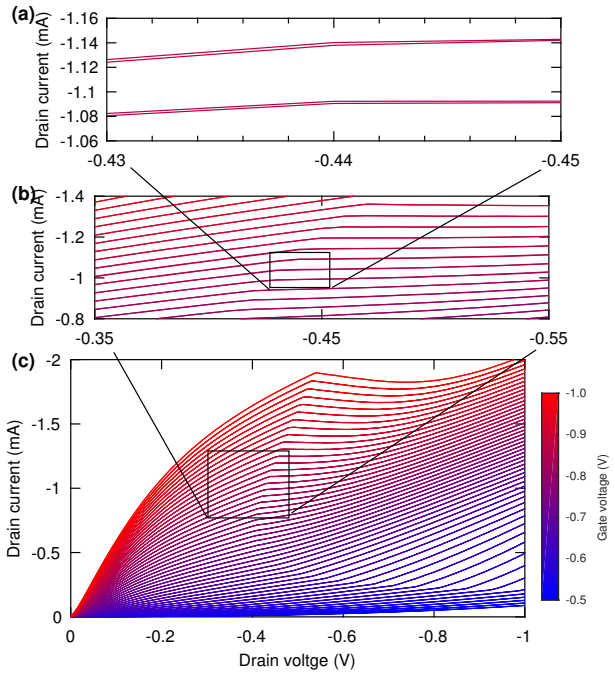

Fig. 2. (Color) Stable transistor characteristics of a Si p-MOSFET at 5 K. (a), (b) Expanded $I_{\rm d}$-$V_{\rm d}$ characteristics. No hysteresis was found. The threshold voltage shift during the measurement was less than 0.1 mV, which proves the quality of the interface of the industrial grade MOS was excellent. (c) $I_{\rm d}$-$V_{\rm d}$ characteristics in the loop measurements. At each $V_{\rm g}$, $V_{\rm d}$ was increased from 0 V to -1 V, and then decreased from -1 V to 0 V in steps of 0.01 V. The root mean square noise level was below 10 pA.

allows the sample temperatures to be varied between 1.6 K and 325 K. The temperature of the sensor is located very close to the sample. The cooling power is up to 1.5 W at 4 K, which is orders of magnitude higher than the maximum power consumption of our device of 2.5 mW. As for the material of the Si substrate, the thermal conductivity increases with decreasing temperature as the temperature decreases below room temperature due to reduced isotope and umklapp scattering of phonons; the thermal conductivity reached its maximum at 28 K, and below that temperature, it decreases due to boundary scattering.[68] The thermal conductivity at 5 K is slightly higher than it is at room temperatures.[68] Therefore, we expected the impact of local temperature increases to be limited for our experiments conducted between room temperature and 5 K. Nevertheless, we have checked the possible impact of the local heating, since our device is on the nanoscale, and it was not easy to determine if the local temperature increase caused the unusual transport properties that were observed.

We used an industry standard semiconductor parameter analyser (B1500, Keysight Technologies) to measure the current-voltage characteristics. First, we performed a loop measurement by sweeping $V_{\rm d}$ from 0 V to -1 V and then sweeping back from -1 V to 0 V at various

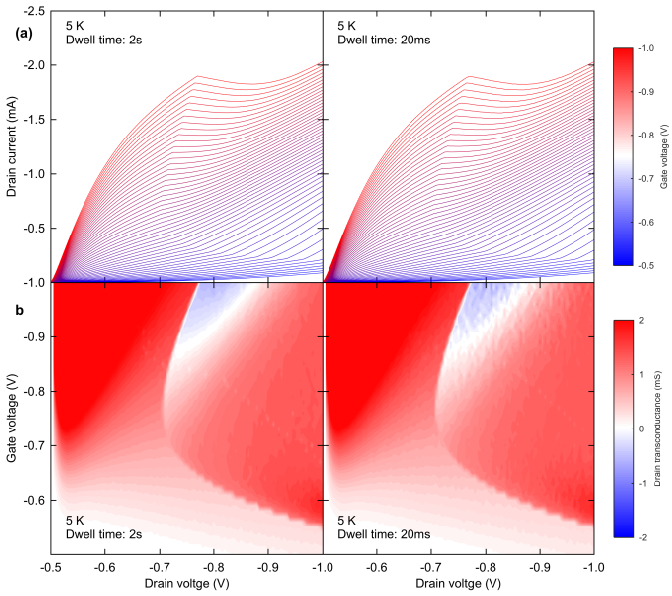

Fig. 3. (Color) High precision measurements of a Si p-MOSFET at 5 K. (a) I_d-V_d characteristics. The I_d sampling time under the application of V_d and V_g was the 2 μs. At a dwelling time of 2 s (20 ms), the measured output data of I_d at each V_d and V_g was the average of 1 M (10 k) sampling points. No qualitative change was found with the dwell time, which means there is no transient behaviour at this time scale. (b) Drain transconductances as functions of V_d and V_g. No qualitative difference with the dwell time was found; however a better signal-to-noise ratio was found in data acquired at a dwell time of 2 s, because of the longer integration time for the measurements at each voltage.

fixed values of V_g (Fig. 2). When the temperature in the device changed during the sweeps, the I_d-V_d curves from the forward and backward sweeps would not coincide, since I_d is highly sensitive to T after the onset of the transition. We confirmed perfect agreements during the sweeps (Fig. 2), and thus, we did not find any evidence of the local heating from the loop measurements.

We have also checked for local heating by changing the sweep speed (Fig. 3). The sampling time to acquire I_d was 2 μs, and we changed the dwell time from 2 s to 20 ms to obtain I_d averaging over 1 M and 10 k sampling points. If the local temperatures changed on this time scale, we should see differences in measurements at different dwell times. However, we could not identify any noticeable changes except for the higher signal-to-noise ratio for the measurement at the longer dwell time (2 s) due to the larger sampling number. Therefore, we excluded the local heating from being the major mechanism of the observed anomalous transport properties.

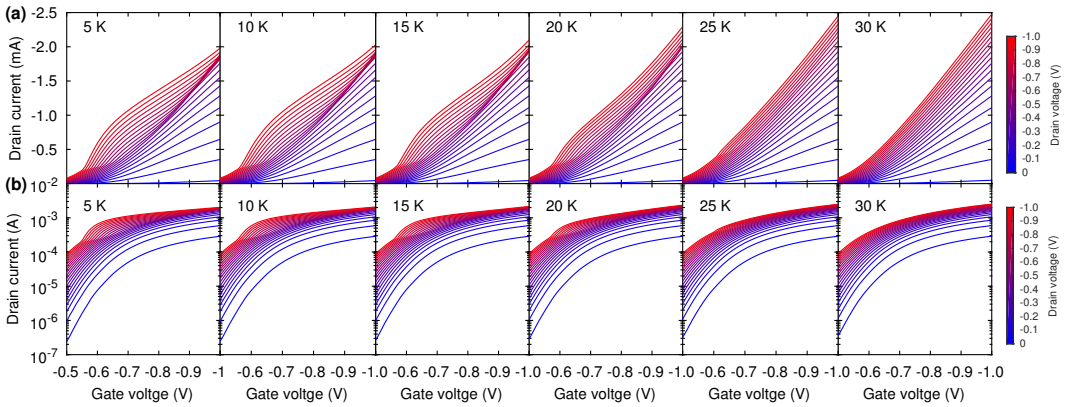

Fig. 4. (Color) Turn-on characteristics of a Si p-MOSFET at low temperatures. (a) Linear scale. (b) Log scale. Anomalous transport properties were observed below 25 K. The increase in I_d at approximately $V_d = -0.6$ V was more prominent at lower temperatures, and the on-current at $V_g = V_d = -1.0$ V continuously decreased, as the temperature was decreased. Clearly, the changes in the $I_d - V_d$ curves cannot be explained by the parallel threshold voltage shift from floating-body effects. New transport mechanisms are responsible to account for the substantial changes at low temperatures.

2.3 Absence of hysteresis or floating-body effects

The changes in the slope of the experimental $I_d - V_d$ curves cannot be explained by conventional floating-body effects due to carrier freezing-out at low temperatures, either, since hysteresis should be accompanied by floating-body effects due to unstable body bias.[69,70] We have carefully confirmed that there is no hysteresis at all over the entire voltage regime; we investigated by loop measurements (Fig. 2) and changing scan speed with the highest accuracy possible in our measurement system (Fig. 3). In fact, the changes in the relationship due to the floating body effects are not usually observed in p-MOSFETs, due to the smaller coefficient expected for the avalanche breakdown; they have only been reported for n-MOSFETs.[69,70] Moreover, the maximum voltage difference was 1.0 V, which is not enough to generate electron-hole pairs by an avalanche breakdown in Si even if the Coulomb interactions were considered[71] because the band gap energy is 1.1 eV. Another extrinsic scenario was the linear kink effect,[72] or in other words, the gate-induced floating body effect,[73] which results from direct tunnelling of holes from the conduction band to produce electrons in the floating n-well due to the charge neutrality. However, this also requires a significant band bending to overcome the band gap energy of Si, and therefore a V_g of more than 1.1 V is required.[72,73] Even if the body bias was affected by the carrier freezing-out, only a small shift in the threshold voltage should be observed, which would result in the parallel shift of the $I_d - V_g$ curves. However, the absence of the floating-body effect is evident in the log scale

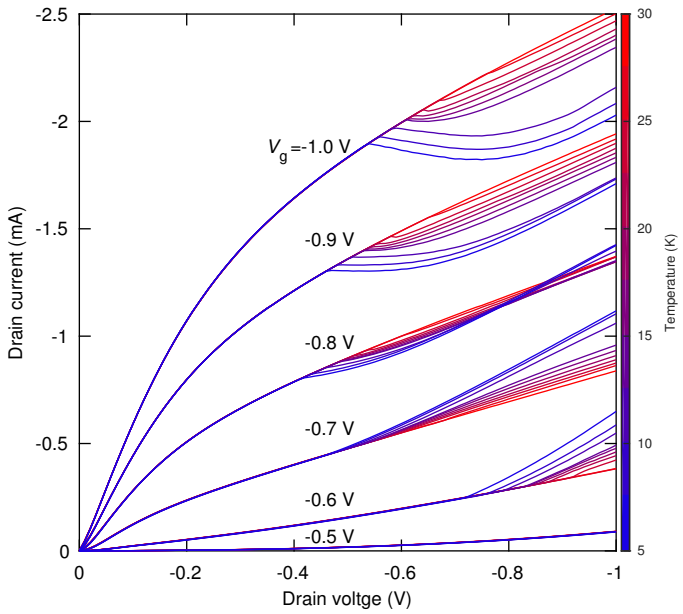

Fig. 5. (Color) Field-induced phase transition in a *p*-MOSFET at low temperatures. Transition from classical to quantum transport. At low fields, the $I_d - V_d$ curves overlapped completely, indicating quasi-ballistic transport with virtually no change in scattering processes with changing temperature. At high fields, the $I_d - V_d$ curves substantially changed with clear changes in slope at the onset of the pinch-off.

plot shown in Fig. 4 (b), where the change in the slope cannot be explained by the threshold voltage shift, and the anomalies appeared as we decreased the temperature (Fig. 4). Below 25 K, we found remarkable discontinuities in the slope of the curves at higher V_g. At lower temperatures, I_d dramatically increased (e.g., at 5 K and $V_d = -1$ V) beyond the conventional subthreshold slope.[9] In addition, we confirmed excellent subthreshold characteristics, a clear threshold, and promising saturation behaviours above 30 K (Fig. 4); however, at temperatures lower than 25 K, we found additional incongruities in the $I_d - V_g$ curves. Therefore, the floating-body effects cannot be responsible for the sudden increase in I_d at 5 K.

2.4 Field-Induced Phase Transition

The dependences of I_d on the drain voltage V_d and temperatures were even more anomalous (Fig. 5). In the subthreshold and linear regimes, all the $I_d - V_d$ curves at various temperatures between 5 K and 30 K completely overlapped, which confirmed the perfect reproducibility of the high-quality industrial grade device with no fluctuations in the body bias or local heating. This means that the mobility was not affected by reduced temperatures, and the device was operating under the quasi-ballistic transport regime. On the other hand, near the saturation regime, where the channel at the drain edge was pinched-off (Fig. 1 (a)), the $I_d - V_d$

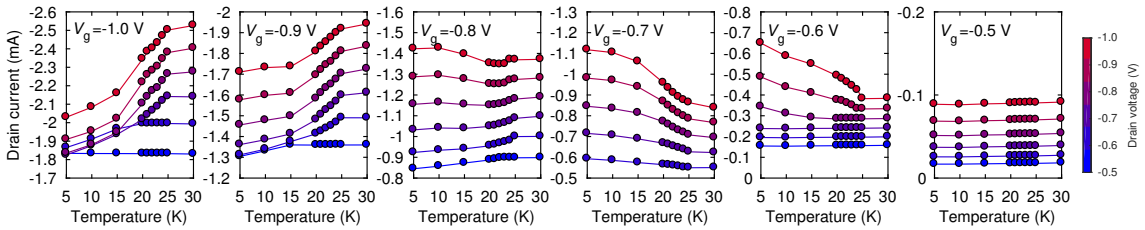

Fig. 6. (Color) Probing hidden order parameters through transport properties. At V_g = -1.0 V and -0.9 V, I_d decreased with decreasing temperatures, while I_d increased at V_g = -0.7 V and -0.6 V. I_d resembled the order parameters seen in statistical physics, and phase transitions are continuous and of the second order. The change in I_d was marginal at V_g = -0.8 V, suggesting the existence of a quantum critical point at a lower temperature. The anomalous behaviours were absent at V_g = -0.5 V.

curves changed dramatically with temperatures (Figs. 5 and 6). We can clearly identify the deviations at the anomalies, and they are suggestive of field-induced phase transitions. As shown by the clear increase in the slope, at V_g = -0.7 V, I_d started to increase substantially against V_d, and the increase in I_d was more prominent as the temperature was further decreased (Fig. 6). At V_g = -0.9 V, I_d decreased with decreasing temperatures (Fig. 6). This is quite unusual in classical transport, since the scattering is always reduced upon reducing temperatures due to the reduction in the thermal fluctuations of phonons, which is the dominant factor impacting the relaxation of the carriers.[9)] The Coulomb scatterings from charged impurities and interface traps, do not contribute substantially in the saturation regime.[9)] Therefore, it is impossible to explain the behaviour of the $I_d - V_d$ curves (Fig. 5) based on a conventional drift-diffusion model. We believe that the phase transition is intrinsically linked to a quantum mechanical transport. By applying strong electric fields, the channel has changed from being $2D$ to $1D$ in nature due to the pinch-off, and the transport properties shifted from the classical transport paradigm to a new quantum transport paradigm, with a field-induced phase transition in between.

In particular, the change in I_d with temperature (Fig. 6) is reminiscent of the development of an order parameter in statistical physics. Our device is a $1D$ mesoscopic system with a finite volume, and therefore, it will not undergo a classical phase transition under the strict definition. In fact, it will be quite challenging to identify order parameters in low dimensional systems, where quantum fluctuations are the major factors impacting the fate of the ground state.[7,42,52,58)] Nevertheless, the behaviours of I_d with temperatures suggest phase transitions are occurring when strong electric fields are applied. I_d itself was continuous when the slopes of the curves against V_d, V_g, and temperatures changed, but the derivatives of I_d have discon-

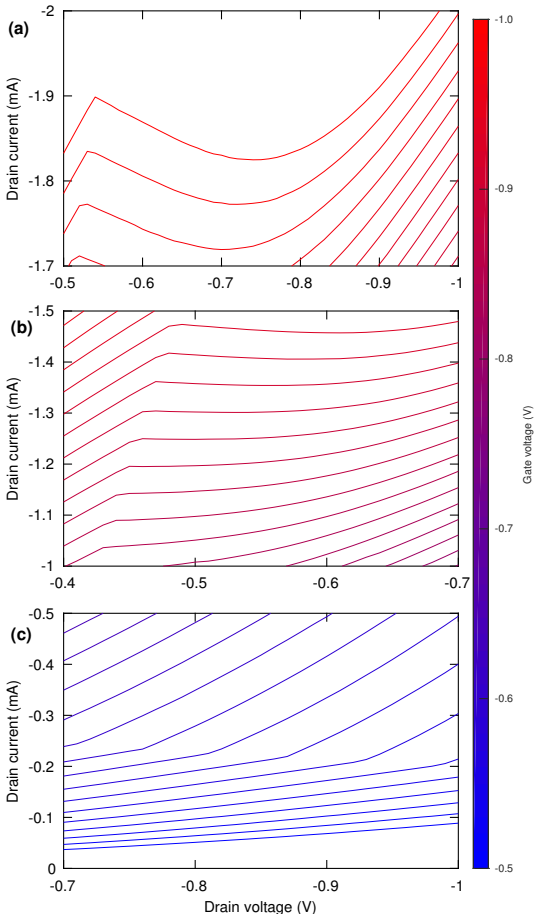

Fig. 7. (Color) Characteristic regimes in anomalous quantum transport at 5 K. (a) Negative differential conductance, which indicates a quantum antiferroelectric state. (b) Current plateau with a pseudo-energy gap. (c) Steep increase of $I_{\rm d}$, indicating a ferroelectric state.

tinuities. Therefore, the transition seems to be continuous in origin and second order (Fig. 6).

There are 3 distinctive regimes in the $I_{\rm d}$-$V_{\rm d}$ curves (Fig. 7), which indicate negative differential conductance (Fig. 7 (a)), current plateau (Fig. 7 (b)), and steep current increase (Fig. 7 (c)), respectively. A remarkable change in the slope accompanies each transition.

The contour plots of $I_{\rm d}$ as functions of $V_{\rm g}$ and $V_{\rm d}$ are shown in Fig. 8. We can roughly identify the phase boundary at the transition; however, $I_{\rm d}$ itself is continuous, which is consistent for a second-order phase transition.

On the other hand, the drain transconductance ($g_{\rm d} = \partial I_{\rm d}/\partial V_{\rm d}$), and the gate transconductance ($g_{\rm g} = \partial I_{\rm d}/\partial V_{\rm g}$) show clear discontinuities at transitions (Fig. 9). Therefore, the observed field-induced phase transitions are of the second order. The anomalies disappear at higher T, indicating the T-induced phase transition is also second order.

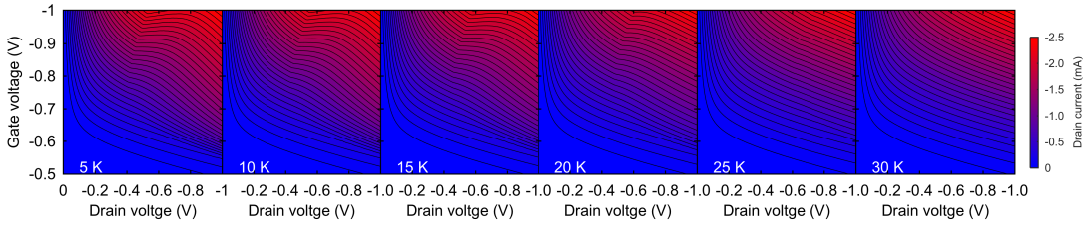

Fig. 8. (Color) Current stability diagram. Classical diffusion limited transport properties at lower voltages change at higher voltages, indicating a new quantum transport mechanism. The phase transitions are less obvious in this contour plot compared with differential conductance due to the continuous nature of the transitions.

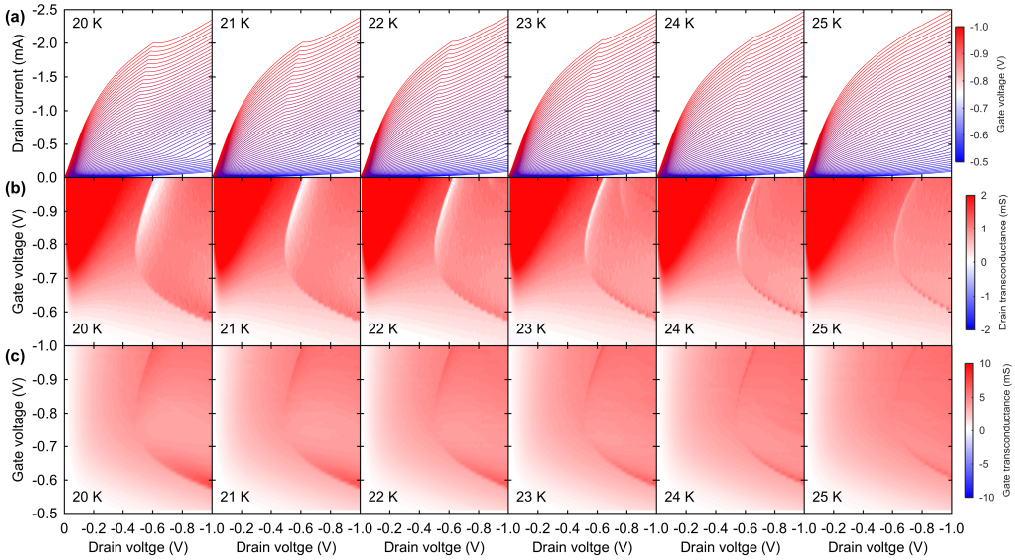

Fig. 9. (Color) Anomalous transport properties of the 1D channel near the transition temperature. (a) Transitions of the transport properties. (b) Drain transconductance, which show the impacts of transverse electric fields. (c) Gate transconductance, which show the doping effects.

We also found an anomalous transport property in the tunnelling gate leakage current (I_g) (Fig. 10). This anomalous increase was found only after the field-induced phase transitions with changes in slope at the phase boundaries (Fig. 10), and the anomaly disappeared at temperatures above the transition temperature. To the best of our knowledge, such an unusual increase in the tunnelling currents at low temperatures has not previously been reported. Notably, the observed I_g was more than 4 orders of magnitudes smaller than I_d, indicating the impacts of I_g on I_d is negligible.

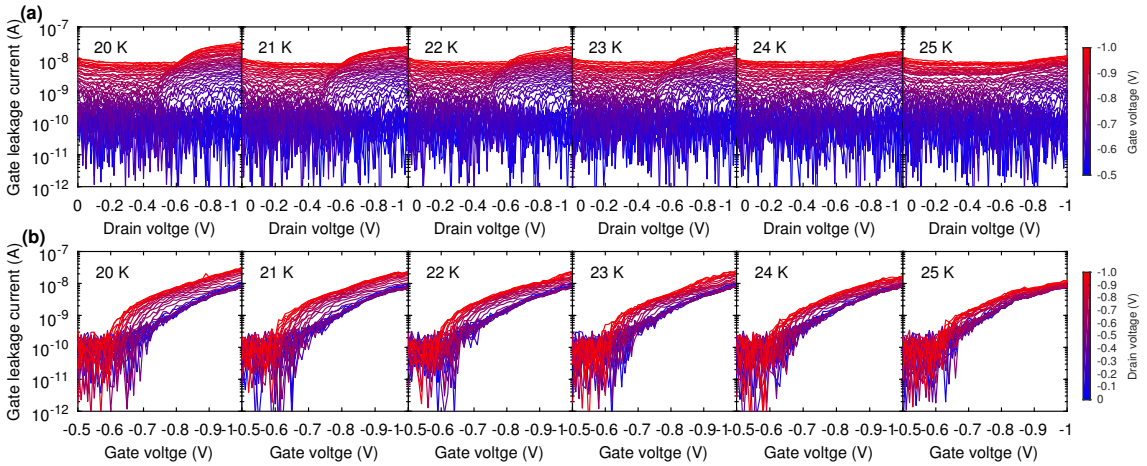

Fig. 10. (Color) Enhanced gate leakage current near phase transition. (a) Field-induced phase transitions and exponential increases in the tunnelling currents at lower temperatures. V_g was held constant at -1 V. (b) Gate-induced phase transitions and exponential increases in the tunnelling currents as the order parameter of the quantum dipole developed. V_d was held constant at -1 V. A substantial increase in the gate tunnelling leakage current was observed in the results of the V_g sweep.

3. Theoretical model

The construction of a comprehensive model to explain our experimental results is beyond the scope of the present paper. Instead, we have tried to qualitatively understand the implications of the data. Here, we will describe the outline of our quantum dipole model, which can be essentially mapped to the same universality class as the attractive Hubbard model and the spin XXZ Heisenberg model in many-body problems.[1–3,7,8,42,52,58,74–76)]

To understand the anomalous transport properties, found in our experiments on *p*-MOSFETs, we have considered applying various single-particle models, including Anderson localisation,[30)] floating-body effects,[72,73)] ballistic transport, and Bloch oscillation[77–79)] (Appendix B). However, none of these models could account for the deviations in slope upon application of the strong electric fields or the temperature dependence, suggesting a phase transition. The unique topological structure of our $1D$ wide channel after the pinch-off was a key observation. Among the various many-body models, $1D$ spin models[7,35–38,42,52)] appeared plausible and applicable,[7,39–48,65–67)] but genuine magnetic orders were unlikely to be expected in Si with sp^3 hybridised orbitals because the Coulomb interactions are not strong, and the one-body band structure model is valid. The only pseudo-spin applicable in this system was a quantum dipole, which would be formed at the extremely thin gate dielectric interface (Fig. 1).

3.1 Derivation of quantum dipole model

In the temperature range of our experiments, carriers were predominantly localised at acceptor impurities due to Anderson localisation.[30] Therefore, we start from the tight-binding Hamiltonian for describing the kinetic energy,

$$H_{\rm kin} = -\sum_{ij\sigma} t_{ij\sigma} c^{\dagger}_{i\sigma} c_{j\sigma} - \sum_{i\sigma} \mu_{\sigma} n_{i\sigma}, \tag{1}$$

where the nearest neighbour transfer energy, t_σ, is determined by the effective mass, m_σ, using $t_\sigma = \hbar^2/(2m_\sigma a^2)$, where a is the average distance between the doped boron (B) atoms in the gate, and $c^{\dagger}_{i\sigma}$ ($c_{i\sigma}$) describes a creation (annihilation) operator for a carrier with the the pseudo spin (σ), corresponding to a a hole in the channel ($\downarrow$) and a depletion (B^-) charge in the gate ($\uparrow$). Of course, the band degeneracies for heavy holes, light holes, and spin-orbit split bands, should be considered as well as real spin degeneracies, but we will ignore them for simplicity. $n_{i\sigma}$ is the number operator at the i-th site. The lowest energy levels for $\uparrow$ and $\downarrow$ are different, because a depletion energy level for B^- ($t_{ii\uparrow} = -E_{\rm B} - 2t_\uparrow$) is located close to the valence band edge ($E_{\rm v}$), and the energy level of a hole ($t_{ii\downarrow} = E_{\rm v} - 2t_\downarrow$) is significantly affected by the band bending due to $V_{\rm g}$ towards the inversion of the channel. In a MOSFET, the electro-chemical potentials in the gate $\mu_\uparrow = \mu_g$ and in the hole channel $\mu_\downarrow = \mu_h = -\mu_n$, which are equivalent to the Fermi levels at zero temperature, can be controlled by $V_{\rm g}$, and the overall charge neutrality condition will be maintained. The opposite sign in $\mu_\downarrow$ is due to the opposite energy axis for holes compared to the electrons in the n-well. In the absence of an external vertical field ($V_{\rm g} = 0$ V), the chemical potential must be aligned, $\mu_\uparrow = \mu_\downarrow = \mu$.

At the MOS interface, the strong Coulomb interaction works between holes ($n_{i\downarrow}$) in the channel and acceptors ($n_{i\uparrow}$) in the gate to form dipoles (Fig. 1 (b)), coming from the the capacitive coupling through the gate oxide. It can be described as the attractive interaction

$$H_{\rm int} = -U \sum_i n_{i\uparrow} n_{i\downarrow}, \tag{2}$$

where $U \sim e^2/(2C_{\rm Q})$ is the charging energy of the quantum dipole. The interaction is attractive, because holes are positively charged, while the acceptors are negatively charged, so that the Coulomb interaction between them must be negative in the atomic scale. This should not be confused with the total energy of the capacitor as a whole in the macroscopic scale, which is always positive to ensure that the free energy is the lowest when the capacitor is not charged. In a MOS capacitor, this condition of zero charge is satisfied at the flat-band voltage[9] and not at $V_{\rm g} = 0$. The total energy of the capacitor is properly taken into account as a boundary condition to satisfy the Gauss's law, $e = C_{\rm Q}|(V_{\rm g} - V_{\rm t})|$. At fi-

nite $V_{\rm g}$, the total capacitive energy, which is the sum of contributions from μ_σ and $-U$, is $e|(V_{\rm g}-V_{\rm t})|-e^2/(2C_{\rm Q})=e^2/(2C_{\rm Q})>0$. Here, the attractive many-body interaction Hamiltonian is describing the local energy gain $(-U)$ of carriers to form quantum dipoles, rather than randomly or uniformly distributed throughout the interface. The quantum capacitance of the dipole, $C_{\rm Q}=C_{\rm ox}S$, is estimated from the gate oxide capacitance $C_{\rm ox}$ and the area S of the charge distribution. When we estimate the gate oxide capacitance $C_{\rm ox}$, we must also consider the $2D$ quantisation of the channel along the direction perpendicular to the surface.[9,23,80] This is because the $2D$ charge centroid of the channel is formed slightly away from the Si/gate insulator interface, and the extra capacitance is added to the total gate capacitance.[9,23,80] Considering the relative dielectric constants of Si ($\kappa_{\rm Si}=11.7$) and SiO_2 ($\kappa_{\rm SiO2}=3.9$), and the average charge centroid being located approximately 2 nm from the interface, the quantum confinement will add an extra effective thickness of $t_{\rm QM}=0.5$ nm to the physical thickness of the gate insulator ($t_{\rm ox}=2.4$ nm). Therefore, we estimated the gate capacitance using $C_{\rm ox}=\epsilon_0\kappa_{\rm SiO2}/(t_{\rm ox}+t_{\rm QM})$, where ϵ_0 is the dielectric constant in a vacuum. By combining the attractive interaction at the MOS interface, we obtain the attractive Hubbard model[2,6,7]

$$H_{\rm kin}+H_{\rm int}=-\sum_{ij\sigma}t_{ij\sigma}c^\dagger_{i\sigma}c_{j\sigma}-\mu\sum_{i\sigma}n_{i\sigma}-U\sum_i n_{i\uparrow}n_{i\downarrow}. \tag{3}$$

In the presence of the external electric field, $\mathbf{E}^{\rm ext}$, we must add a term of the dipole interaction, $\mathbf{P}\cdot\mathbf{E}$,

$$H_{\rm ext}=-E^{\rm ext}_y\sum_i P^y_i-E^{\rm ext}_z\sum_i P^z_i, \tag{4}$$

to the Hamiltonian, where $\mathbf{E}^{\rm ext}$ is obtained as

$$E^{\rm ext}_x = 0 \tag{5}$$

$$E^{\rm ext}_y = -\frac{V_{\rm d}}{L} \tag{6}$$

$$E^{\rm ext}_z = -\frac{V_{\rm g}-V_{\rm t}}{t_{\rm ox}}, \tag{7}$$

where $V_{\rm d}$ is the drain voltage and $V_{\rm t}$ is the threshold voltage for the transistor. Here, the dipole operators are defined as

$$P^x_i = \frac{d}{2}(c^\dagger_{i\uparrow}c^\dagger_{i\downarrow}+c_{i\downarrow}c_{i\uparrow}) \tag{8}$$

$$P^y_i = \frac{d}{2i}(c^\dagger_{i\uparrow}c^\dagger_{i\downarrow}-c_{i\downarrow}c_{i\uparrow}) \tag{9}$$

$$P^z_i = \frac{d}{2}(n_{i\uparrow}+n_{i\downarrow}-1), \tag{10}$$

where the quantum dipole moment is $d = et_{\rm ox}$. It is straightforward to check the commutation relationship

$$[P_i^\alpha, P_i^\beta] = id\epsilon_{\alpha\beta\gamma}P_i^\gamma, \tag{11}$$

whereα, β, and γ are one of the components (x, y, and z), and $\epsilon_{\alpha\beta\gamma}$ is the Levi-Civita symbol, which is a fully antisymmetric tensor giving 1 (-1) for the even (odd) commutation of $(\alpha,\beta,\gamma) = (x,y,z)$ and 0 for otherwise.[7)] The definition of the polarisation operator, P_i^α, can be checked by the famous particle-hole transformation only for 1 spin component, which would map the attractive Hubbard model onto the repulsive Hubbard model,[7,81)] and P_i^α is consistent with the standard definition of the spin operator.

We have derived the $SU(2)$ commutation relationships of polarisation operators, which are essentially the same as the spin commutation relationship, except for one noticeable difference; that the constant of the dipole moment can be artificially designed by choosing the gate oxide thickness in fabrication technologies. On the other hand, in spin systems, the spin angular moment is naturally quantised in the units of fundamental Dirac's constant $\hbar$, which cannot be changed. Therefore, we can tune the impacts of quantum effects on polarisations by engineering. Interestingly, we expect the thicker the oxide thickness, the larger the quantum effects, since the larger d corresponds to the larger $\hbar$. This means that the quantum dipoles are easier to allow quantum fluctuations, if the dipole moment is larger. Practically, however, quantum dipoles will not be well-defined, if $t_{\rm ox}$ is too thick compared with a, so that the appropriate choice of $t_{\rm ox}$ and carrier densities would be important.

We briefly mention about the nature of quantum dipoles using fundamental $SU(2)$ states at each lattice site. If the B impurity site is doubly occupied, the quantum dipole exists, which corresponds to the dipole up state

$$|\uparrow\rangle_i = c_{i\uparrow}^\dagger c_{i\downarrow}^\dagger |0\rangle \tag{12}$$

$$= |1\rangle_i^{\rm g}|1\rangle_i^{\rm c}, \tag{13}$$

and the empty state corresponds to

$$|\downarrow\rangle_i = |0\rangle_i^{\rm g}|0\rangle_i^{\rm c}. \tag{14}$$

These can be confirmed by calculating $P_i^z|\uparrow\rangle_i$ and $P_i^z|\downarrow\rangle_i$ in the standard $SU(2)$ matrix formulation as

$$\frac{d}{2}\begin{pmatrix} 1 & 0 \\ 0 & -1 \end{pmatrix}\begin{pmatrix} 1 \\ 0 \end{pmatrix} = \frac{d}{2}\begin{pmatrix} 1 \\ 0 \end{pmatrix}, \tag{15}$$

316

$$\frac{d}{2}\begin{pmatrix} 1 & 0 \\ 0 & -1 \end{pmatrix}\begin{pmatrix} 0 \\ 1 \end{pmatrix} = -\frac{d}{2}\begin{pmatrix} 0 \\ 1 \end{pmatrix}. \tag{16}$$

317 Therefore, $c^\dagger_{i\uparrow}c^\dagger_{i\downarrow}$ works as a standard ladder operation to increase the quantum dipole moment.
318 Similarly, the quantum superposition state between $|\uparrow\rangle_i$ and $|\downarrow\rangle_i$ corresponds to the dipole
319 states alining to the longitudinal direction x

$$|\rightarrow\rangle_i = \tfrac{1}{\sqrt{2}}(|\uparrow\rangle_i + |\downarrow\rangle_i), \tag{17}$$

$$|\leftarrow\rangle_i = \tfrac{1}{\sqrt{2}}(|\uparrow\rangle_i - |\downarrow\rangle_i), \tag{18}$$

320 and those states aligning along the horizontal direction y are

$$|\circlearrowleft\rangle_i = \tfrac{1}{\sqrt{2}}(|\uparrow\rangle_i + i|\downarrow\rangle_i), \tag{19}$$

$$|\circlearrowright\rangle_i = \tfrac{1}{\sqrt{2}}(|\uparrow\rangle_i - i|\downarrow\rangle_i), \tag{20}$$

321 which are easily checked to be eigenstates of P^x_i and P^y_i, respectively. According to the $SU(2)$
322 algebra, we can describe arbitrary states by superpositions of $|\uparrow\rangle_i$ and $|\downarrow\rangle_i$ states.

323 Next, we can check the validity of the total Hamiltonian,

$$H_{\rm kin} + H_{\rm int} + H_{\rm ext} = -\sum_{ij\sigma} t_{ij\sigma}c^\dagger_{i\sigma}c_{j\sigma} - \mu\sum_{i\sigma} n_{i\sigma} - U\sum_i n_{i\uparrow}n_{i\downarrow} - E^{\rm ext}_y\sum_i P^y_i - E^{\rm ext}_z\sum_i P^z_i, \tag{21}$$

324 in the weak coupling limit, where the charge density is uniformly distributed to give the
325 average filling $\langle n_{i\sigma}\rangle = n_\sigma$, while U and $E^{\rm ext}_z$ dominate over $t_{ij\sigma}$. In this classical mechanical
326 case, the average energy is obtained as

$$E^{\rm CM} = \frac{\langle H\rangle}{N_{\rm L}} \tag{22}$$

$$= -(V_{\rm g} - V_{\rm t})en_\sigma - Un^2_\sigma, \tag{23}$$

327 where $N_{\rm L}$ is the total number of the lattice sites, i.e., the number of B impurities at the MOS
328 interface above the channel. By assuming the first derivative is zero,

$$\frac{\partial E^{\rm CM}}{\partial n_\sigma} = 0, \tag{24}$$

329 we obtain

$$en_\sigma = -C_{\rm Q}(V_{\rm g} - V_{\rm t}) \tag{25}$$

$$= C_{\rm Q}|(V_{\rm g} - V_{\rm t})|, \tag{26}$$

330 which shows the local validity of the Gauss's law. Therefore, our Hamiltonian covers the
331 standard limit of the classical capacitance, in which the ordering of dipoles is not considered.

In a MOSFET, the charge neutrality is always satisfied

$$n_\uparrow = n_\downarrow. \tag{27}$$

We can also define the filling fraction n as

$$n = n_\uparrow + n_\downarrow, \tag{28}$$

which gives the average number of carriers at each lattice site. If the half of the lattice sites are occupied by dipoles, we obtain $n = 1$, which is in agreement with the standard definition of the filling in the Hubbard model.[7,74,75]

In the strong coupling limit, where U is much larger than $t_{ij\sigma}$, the attractive Hubbard model can be mapped to the quantum *AF-electric* Heisenberg XXZ model[4,82]

$$H = J^{xy} \sum_{\langle ij \rangle} (P_i^x P_j^x + P_i^y P_j^y) + J^z \sum_{\langle ij \rangle} P_i^z P_j^z - E_z \sum_i P_i^z - E_y \sum_i P_i^y, \tag{29}$$

where $J^{xy} = 4t_\uparrow t_\downarrow/(Ud^2)$, $J^z = 2(t_\uparrow^2 + t_\downarrow^2)/(Ud^2)$, and the sum will run over all the nearest neighbour bonds. This XXZ model describes the local interaction between quantum dipoles. AF ordering is energetically preferred for the exchange interaction, since dipoles can fluctuate quantum mechanically. On the other hand, Ising-like ferroelectric ordering is also expected, if the external electric fields are large. Here, the horizontal effective electric field was estimated as $E_y = (V_\mathrm{d} - V_\mathrm{c})/L$, where V_c is the critical voltage determined by experiments, and the vertical electric field

$$\begin{aligned} E_z &= E_z^\mathrm{ext} + E_z^\mathrm{chem} && (30)\\ &= -\frac{V_\mathrm{g} - V_\mathrm{t}}{t_\mathrm{ox}} + \mu\frac{2}{d} && (31)\\ &= \frac{2}{d}\left(\mu + U\frac{n}{2}\right), && (32) \end{aligned}$$

where E_z^chem is the effective field coming from the chemical potential, and we assumed the Gauss's law (26). This is consistent with the known result[7,75,82,83] at the half-filling ($n = 1$) and shows $\mu = -U/2$ and $E_z = 0$, which must be satisfied due to the particle-hole symmetry of the Hubbard model.[83] Notably, the effective field in the dipole model is different from the external field.

To understand our experimental data, we considered the above quantum dipole model, which describes the dipole, formed at the extremely thin gate dielectric interface due to the strong vertical electric field (Fig. 1 (b)). Inversion holes would be trapped by remote charges in the gate[84] to form dipoles at low temperatures because of the carrier freezing-out due to the intrinsic Anderson localisation.[30] Therefore, unlike excitons in bilayer quantum hall sys-

tems[3)] and exciton-polariton condensates in quantum wells,[5)] quantum dipoles cannot move freely. The interaction between dipoles is short-range, meaning the sum over i and j will be limited to all the nearest neighbour bonds.[7)] Our quantum dipole model is equivalent to the spin model for magnetism, and thus, we can apply various theories that have been developed for spin systems to understand the anomalous transports observed in this system.

3.2 Mean field theory

We have solved the above Heisenberg XXZ model using a mean field theory, which is justified under the application of high electric fields.[7,83)] In this limit, the Heisenberg model simply becomes the Ising model, and the spin is aligned to the easy axis along the effective electric field. We assumed the most simplest situation without anisotropy in exchange interactions, $J^{xy} = J^z$, and the energy scale was set up according to $J = zJ^{xy}d^2/4$, where z is number of the nearest neighbour sites. The energy scales of the effective fields were estimated by $h_y = dE_y/2$ and $h_z = dE_z/2$. The energy scale of h_y is especially important since it is approximately $et_{\rm ox}V_{\rm d}/2L$, which should be on the order of $J \sim k_{\rm B}T_{\rm c}$, where $k_{\rm B}$ is the Boltzmann constant. In other words, the molecular field from the dipole will generate the effective drain voltage change on the order of $J/e\dot{(}2L/t_{\rm ox})$, and the large ratio, $2L/t_{\rm ox} \sim 38$, is the origin of the significant change in currents from the onset of the dipole ordering.

The typical solutions of the Ising model are shown in Fig. 11. We have assumed the canonical ensemble, where the density of carriers is not dependent on temperatures at fixed voltages, and we solved to determine the chemical potential self-consistently (Fig. 11 (b) and 11 (c)). The applied effective field was set as negative since the number of empty sites (down dipole) was larger than the number of occupied sites (up dipole) for fillings less than the half-filling. Near the half-filling, we found the AF ordering below the transition temperature, and no AF ordering was observed far away from $n = 1$ (Fig. 11 (a)). Due to these ordering, the horizontal effective field was screened by the AF ordering, but it was enhanced by the ferroelectric ordering (Fig. 11 (h)).

3.3 Transport characteristics

According to the standard drift-diffusion model,[9)] the values of the drain current $I_{\rm d}$ in the linear and the saturation regions are given by

$$I_{\rm d} = Wv_yC_{\rm ox}\left(V_{\rm g} - V_{\rm t} - m\frac{V_{\rm d}}{2}\right), \tag{33}$$

where the body factor m is a value close to 1, and the factor of $1/2$ is coming from the reduction of the average carrier concentration by the application of $V_{\rm d}$ (Fig. 12). We have

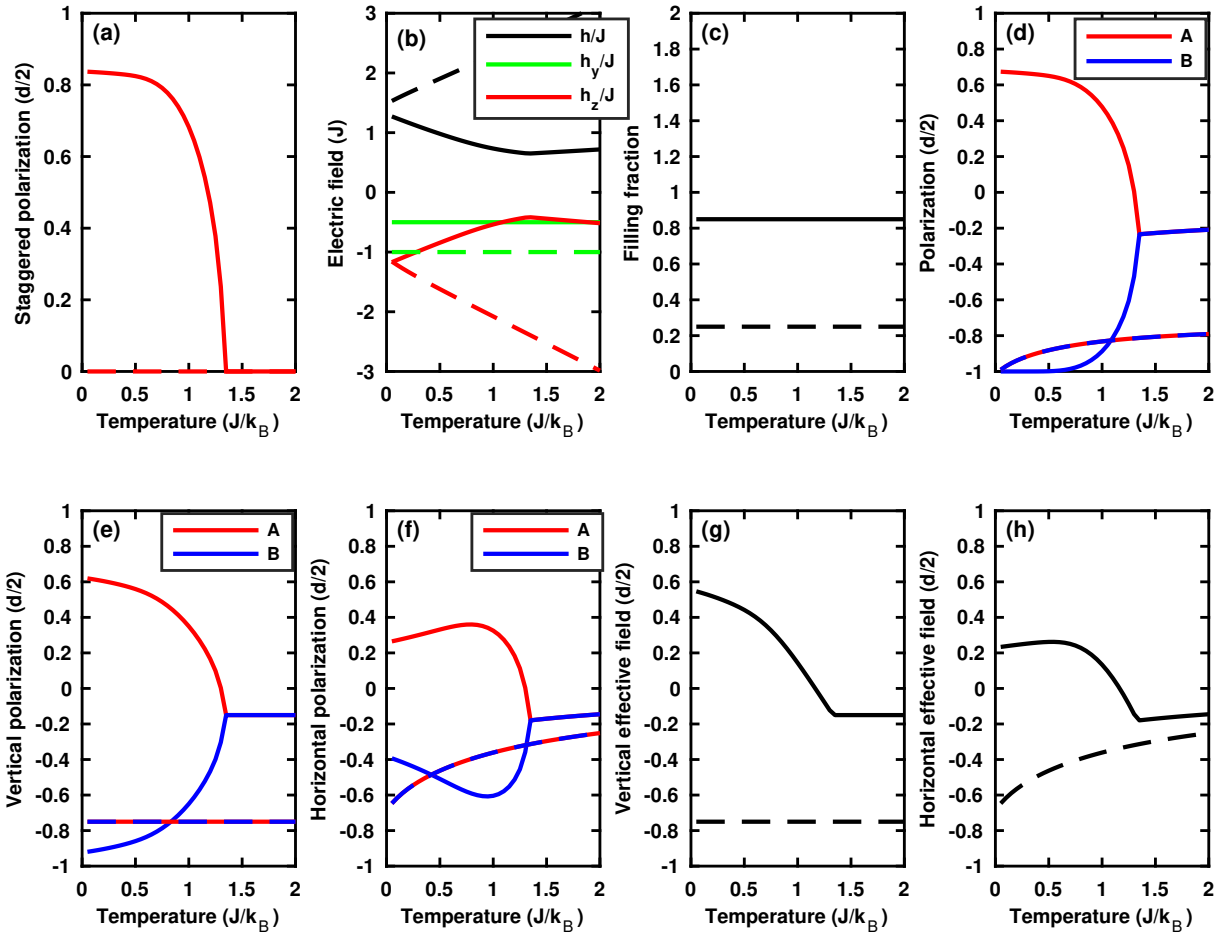

Fig. 11. (Color) Mean field solution for a dipole system. The solid lines are the results for $h_y = -0.5J$ at $n = 0.85$ and represent the AF ordering, and the dotted lines are results for $h_y = -J$ at $n = 0.25$ and represent the dipole polarised ferroelectric ordering. The red (blue) curves show the results for A (B) bipartite lattice. (a) Staggered AF moment. (b) Self-consistently obtained effective fields. (c) Filling fraction, which shows the consistency of the calculations. (d) Polarisation of the dipole along the applied effective field. (e) Vertical polarisation of the dipole. (f) Horizontal polarisation of the dipole. (g) Average vertical molecular field from the dipole. (h) Average horizontal molecular field from the dipole.

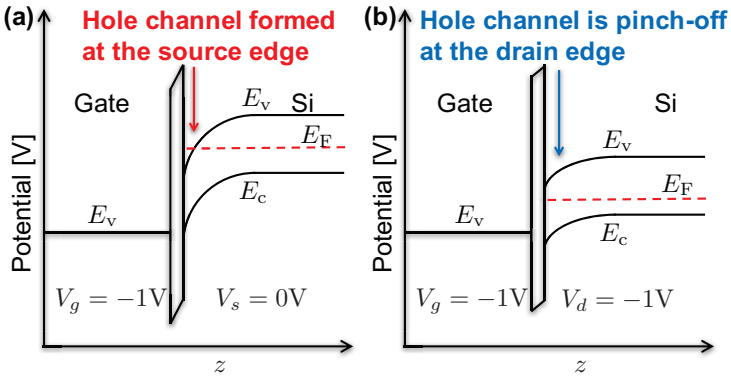

Fig. 12. (Color) Schematic band profile. (a) Near the source edge. (b) Near the drain edge. The carrier concentrations near the source and drain edges are different due to the application of V_d.

used an empirical velocity saturation model,[9] and the drift velocity, v_y, is given by

$$v_y = \mu_{\rm eff} \frac{|E_y|}{1 + |E_y|/E_{\rm c}}, \tag{34}$$

where $\mu_{\rm eff}$ is the effective hole mobility and the critical electric field is $E_{\rm c} = v_{\rm sat}/\mu_{\rm eff}$ at a saturation velocity of $v_{\rm sat} = 7 \times 10^6$ cm/s. We could calculate parameters such as $\mu_{\rm eff}$ and $V_{\rm t}$ by the fitting to the experimental data at 30 K.

3.4 Connection between XXZ model and transport properties

We have discussed about the longitudinal ordering of quantum dipoles by an XXZ model, but the transport properties were measured along the transverse direction perpendicular to the $1D$ channel. The properties of quantum dipoles can be probed by the transport through the effective fields changed by the on-set of phase transitions. After the field-induced phase transition, E_y in Eq. (34) is replaced with the mean-field including the molecular field

$$E^y_{\rm MF} \quad = \quad E_y - \sum_{\langle j \rangle} J^{xy} \langle P^y_j \rangle, \tag{35}$$

which is calculated by the Heisenberg/Ising model. Examples of the calculated effective $E^y_{\rm MF}$ are shown in Fig. 11 (h). The AF ordering reduces $E^y_{\rm MF}$, while ferroelectric ordering increases $E^y_{\rm MF}$. Therefore, the carrier velocity v_y and thus $I_{\rm d}$ would be significantly affected by phase transitions. The energy scales estimated from experiments are shown in Appendix C.

3.5 Simulated results for the impact of quantum dipole on carrier transport

Fig. 13 (a) shows a calculated typical calculated drain current ($I_{\rm d}$) as a function of the drain voltage ($V_{\rm d}$). $I_{\rm d}$ saturates at the pinch-off (Fig. 1 (a)), and $I_{\rm d}$ does not increase with further increases in $V_{\rm d}$ due to the reduction in the carrier concentration at the drain edge.[9] However, according to the velocity saturation model,[9] the carrier velocity is not actually saturated at the pinch off (Fig. 13 (b)). Therefore, there is room for the $I_{\rm d}$ to increase with an increase in the velocity from the molecular dipole field even after the pinch-off. In fact, if the filling fraction (n) is low under the application of a modest gate voltage ($V_{\rm g}$), $I_{\rm d}$ increases after the onset of the dipole-polarised ferroelectric state (Fig. 13 (c)). Experimentally, this corresponds to the observed sharp increase of $I_{\rm d}$ against $V_{\rm d}$ (Fig. 7 (c)). In contrast, if the carrier concentration is closer to the half filling ($n = 1$), on the other hand, $I_{\rm d}$ decreased upon increasing $V_{\rm d}$ due to the screening of electric field by the AF-electric ordering (Fig. 13 (d)). Therefore, the negative differential conductance is expected from the AF ordering, while the further increases in $V_{\rm d}$ will align the staggered moment along the field, which increases $I_{\rm d}$ at higher $V_{\rm d}$ (Fig. 13 (d)). Experimentally, the negative differential conductance was observed

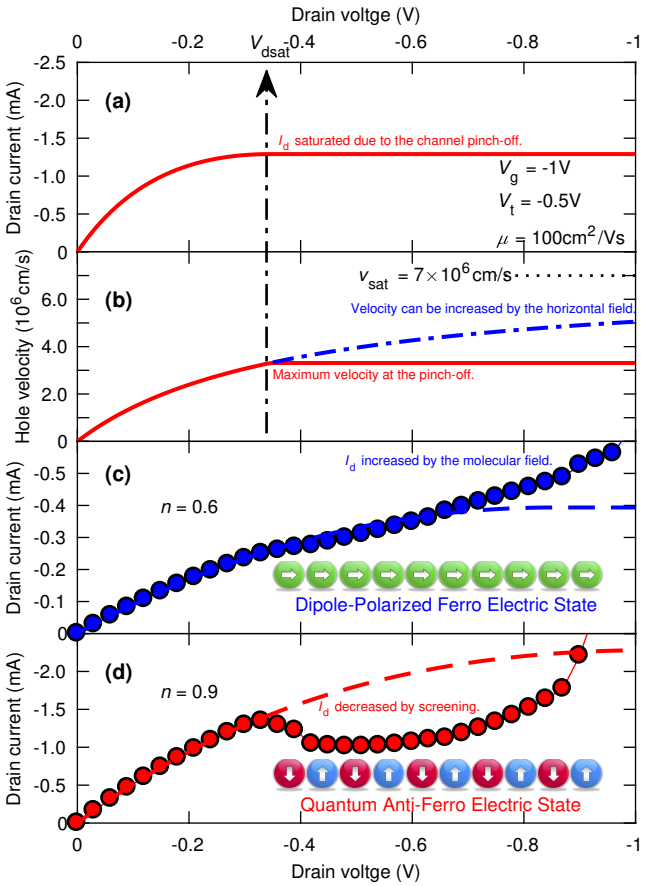

Fig. 13. (Color) Simulated impact of quantum dipoles on the transport properties in a p-MOSFET. (a) Typical $I_d - V_d$ behaviour near the saturation. (b) Velocity saturation model. The dotted line shows the velocity curve without a pinch-off. (c) Simulated I_d with the enhanced velocity from the dipole molecular field. The dotted line shows I_d without the ferroelectric ordering. (d) Simulated I_d with the reduced velocity from the screening of the electric field by antiferroelectric ordering. The dotted line shows I_d without the antiferroelectric ordering.

under the application of the larger V_g (Fig. 7 (a)).

We have further simulated $I_d - V_d$ characteristics by using extracted experimental parameters. The calculated results (Fig. 14) are in reasonable agreement with the experimental trends, regardless of the mean field approximation.

Above 30 K, the dipoles are not ordered, so the transport is determined by standard drift and diffusion. Below 25K, phase transitions are expected due to the ordering of the dipoles. In particular, if the carrier concentration is high, AF ordering is expected, and the staggered polarisation will develop as we decreased T (Fig. 11 (a)). Due to this AF ordering, the negative differential conductance is expected at lower T (red curves in Fig. 14), which is consistent with the extended AF regions experimentally observed in the drain transconductance (Fig. 9). We could also successfully simulate ferroelectric states when the carrier concentration is

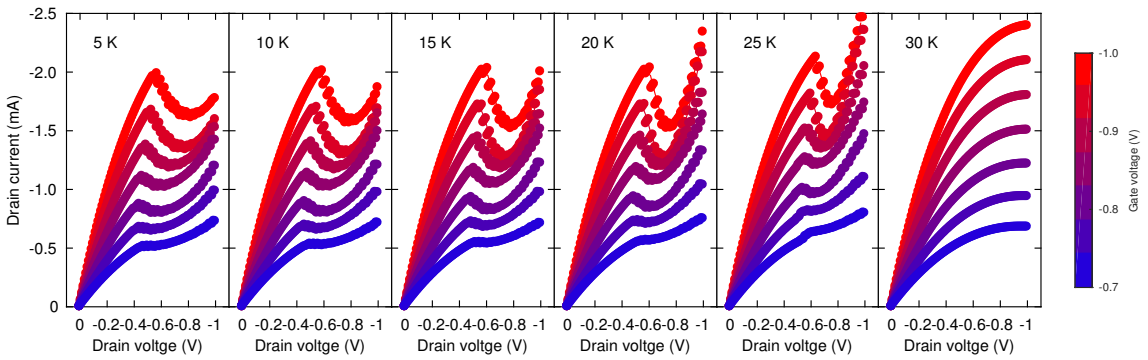

Fig. 14. (Color) Simulated transport properties for a Si *p*-MOSFET. The experimental parameters such as mobility and the threshold voltage were extracted from experimental data at 30 K by least square fitting. The critical drain voltage for the field-induced transition was also extracted from experimental data at each temperatures. Then, the molecular dipole fields were calculated from the mean-field theory of the Heisenberg model, and a standard velocity saturation model and transistor formulas were used to calculate $I_{\rm d}$-$V_{\rm d}$ behaviour. The AF-electric ordering resulted in the negative differential conductance, while the ferroelectric ordering enhances the carrier velocity.

low (blue curves in Fig. 14). In these states, dipoles are polarised due to the strong transverse fields coming from $V_{\rm d}$. These dipoles will produce the effective molecular field (dotted line in Fig. 11 (h)) to increase the carrier velocity.

4. Results and Discussion

4.1 Ferroelectric and antiferroelectric states

There are at least three important regimes in our $I_{\rm d} - V_{\rm d}$ curves (Fig. 15). At lower $V_{\rm g}$, we found an abrupt increase of $I_{\rm d}$ with a kink at the threshold (Fig. 15 (c)). We assigned this phase to be a quantum ferroelectric phase, which was induced by the high electric field, $E_{\rm y}$, due to the scaled channel length (L). In this state, the quantum dipole is aligned along the y direction, and the neighbouring dipoles increase the effective electric field. This molecular mean field will increase the average dipole moment, $\langle P^y \rangle$, and $I_{\rm d}$ will increase accordingly. We confirmed this hypothesis using simulations (Fig. 13 (c)). In this phase, the $U(1)$ symmetry in the XY plane is broken, and the none-zero off-diagonal order parameter corresponds to the BEC[4,82] of the excitons in our 1D channel. The lifetime of our exciton are long due to the physical separation provided by the gate oxide and the indirect band gap character of Si. This paring state is similar to the Cooper pair in a superconductor, but our composite particle has neutral charge instead of the $\pm 2e$ for the Cooper pair.

The next important feature is the negative differential conductance observed at the higher $V_{\rm g}$ (Fig. 15 (a)). This is quite unusual since $I_{\rm d}$ usually continuously increases against $V_{\rm d}$ when

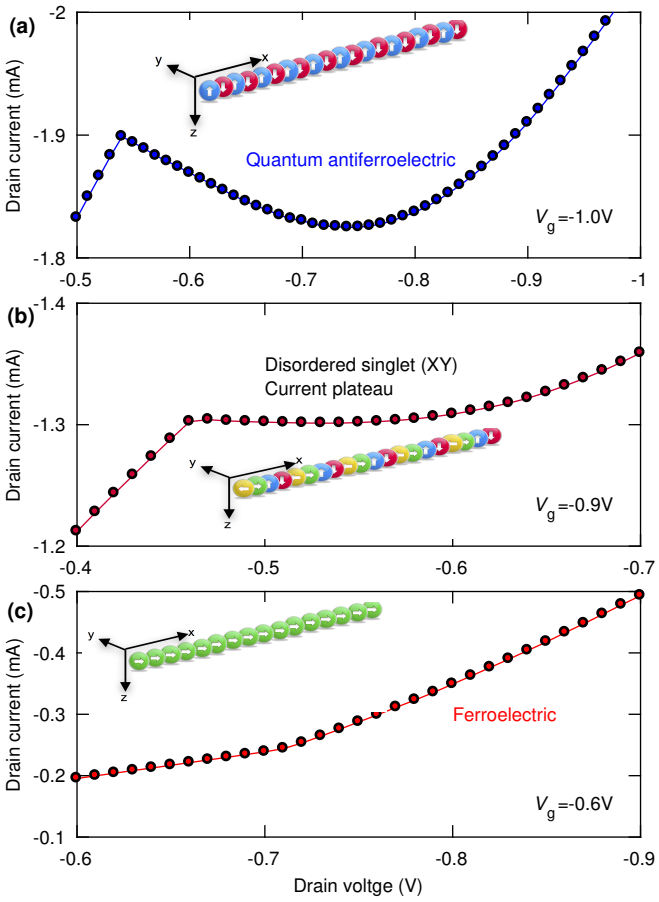

Fig. 15. (Color) Quantum states in the 1D channels. (a) Quantum antiferroelectric state. The negative differential conductance was observed due to the charge ordering along the source edge. (b) New current plateau. Disordered singlet states would be responsible for the emergence of the energy gap in the system. (c) Ferroelectric state. This state corresponds to the Bose-Einstein condensation of excitons at the MOS interface.

the drain edge of the channel becomes pinched-off. According to our quantum dipole model, we can attribute the quantum AF-electric state due to the enhanced effect of J^z (Fig. 13 (d)). In this state, the dipole order along z is expected, and the dipoles cannot move freely inside the XY plane. In fact, dipoles occupy alternating sites and leave every other site unoccupied, which means that this state corresponds to the charge-density-waves (CDWs) state.[7] Due to the local singlet formation along z, the dipole moment along y was reduced, which caused $I_{\rm d}$ to decrease as well. However, if we apply an even higher E_y, the energy scale is increased by the external field, so the dipole begins to align along the y-direction, which caused the increase of $I_{\rm d}$ at higher $V_{\rm d}$.

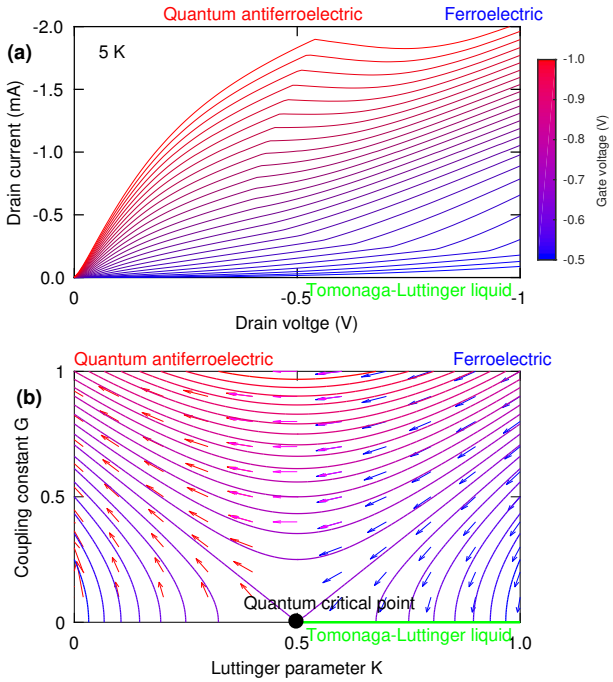

Fig. 16. (Color) Comparisons of transport characteristics with renormalisation flows. (a) Experimental $I_{\rm d}-V_{\rm d}$ data of p-MOSFET at 5K. (b) Theoretical renormalisation flows using the XXZ model. As the energy scales are reduced by reducing $V_{\rm d}$, ferroelectric states are renormalised to quantum antiferroelectric states, if $V_{\rm g}$ is sufficiently large. If the carrier concentration is low, the state is renormalised to a Tomonaga-Luttinger liquid state.

4.2 Renormalisation group flow

We can confirm above pictures by applying the renormalisation group flow,[7,38,67] known for the XXZ model (Fig. 16). The mean field approximation cannot be justified when the electric fields are weak and the quantum fluctuations are large.[2,7,67,74–76] In that interesting intermediate regime, the low energy properties of the XXZ Heisenberg model are described by the sine-Gordon model, the properties of which can be explained by the renormalisation group theory.[2,7,67,74–76] Assuming the Luttinger parameter (K) and the coupling constant (G), the system can be renormalised by the change in the length (l) scale as

$$\frac{dK}{dl} = -cG^2 \tag{36}$$

$$\frac{dG}{dl} = 2(1-2K)G, \tag{37}$$

where c is a numerical constant. The flows are described by simple hyperbolic curves that satisfy

$$G^2 - \frac{(2K-1)^2}{c} = c_0, \tag{38}$$

Table I. Comparisons among BKT, Quantum Hall, and Quantum dipole systems.

System	BKT	Quantum Hall	Quantum Dipole
Device	Superfulid films	Hall bar	p-MOSFET
Materials	He, Al	Si, GaAs, Graphene	Si
Dimension	$2D$	$2D$ and $1D$ at the edge	$1D$
Field	Many-body interaction	Magnetic field (> 10 T)	Electric field (> 1 MV/cm)
Localization	Effective local spin	Impurities in a channel	Remote charges in a gate
Quantisation	Spin	Landau level	Dipole
Excitation	Charges	Fractional charges	Magnetic monopole
Vortex	Binding/Un-binding	Composite fermions/bosons	Excited in space-time
Phase transition	Temperature induced	Field induced	Temperature/field induced
Hamiltonian	XY	Chern-Simons	XXZ
Characteristics	Universal jump at T_c	Plateau in Hall conductance	Plateau in drain currents
	Topological phases	Edge states	Negative conductance
	No long-range order	Chiral Luttinger liquid	Exciton BEC

where c_0 is the integration constant. The typical renormalisation flow at $c = 2$ is described in Fig. 16. Our $I_d - V_d$ characteristics are resemble to these flows. Our $I_d - V_d$ curves are essentially equivalent to the change in the energy scales and thus correspond to the renormalisation group flow. This means that the quantum AF-electric state is favourable when the energy scale is reduced at higher doping concentrations. By increasing the energy scale with increasing V_d, the state could shift from AF-electric to ferroelectric states opposite to the low energy scaling flow. The comparisons with other systems are summarised in Table I.

4.3 Plateau

The last critical feature was a new current plateau, which was discovered at intermediate V_g (Fig. 15 (b)), where a disordered singlet phase or an XY phase is expected.[7)] We think this phenomenon is related to the magnetisation properties of the spin models upon the application of the transverse magnetic fields.[7,39,42,44–47)] The emergence of plateaus suggests the formation of the energy gap between the ground state and the excited state, which is extremely important, since it is intricately related to the new state of matter as an order parameter, as seen in superconductivity, magnetisation, and integer/fractional quantum Hall effects. In particular, field-induced magnetisation plateaus were theoretically predicted in the frustrated spin half systems.[44–46)] This means that the formation of the Haldane gap in half-integer spin systems occurs under certain conditions,[44–46)] where the gapless excitations were originally predicted, which is in contrast to the gapped excitation in integer spin systems.[39)]

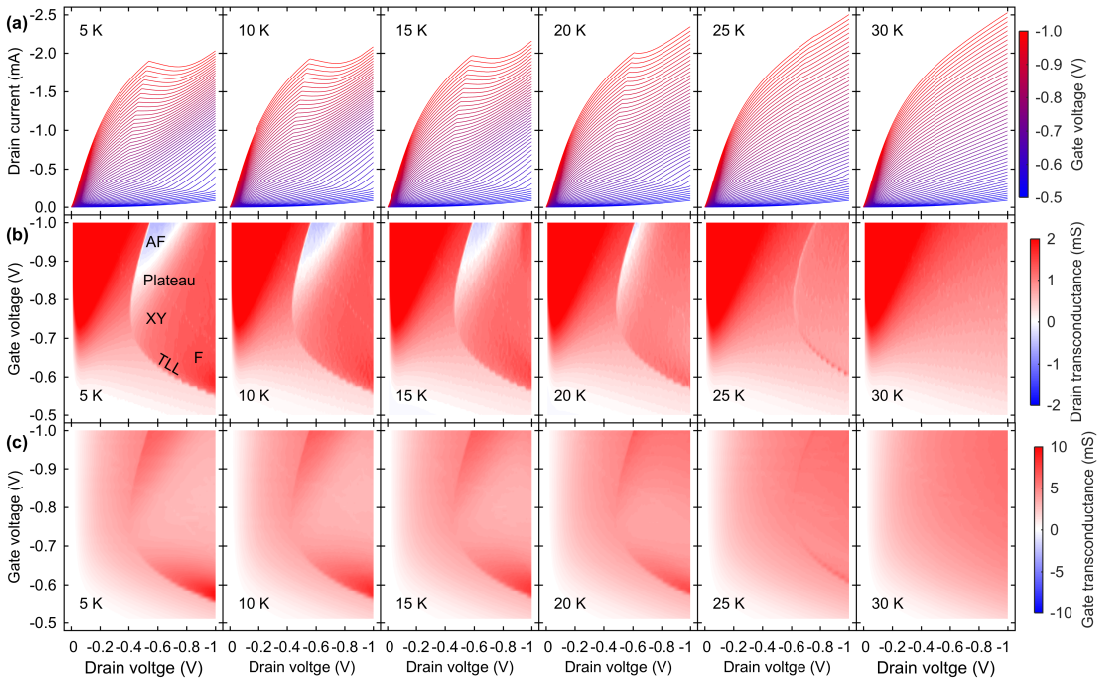

Fig. 17. (Color) Phase diagrams of the 1D channel under strong electric fields. (a) Changes in the transport properties against energy scales similar to the renormalisation flow. (b) Field-induced transitions probed by $g_{\rm d}$ within the quantum antiferroelectric (AF), plateau, XY, and ferroelectric (F) regimes. Tomonaga-Luttinger liquid (TLL) properties are expected at the lower boundary. (c) Impact of carrier doping in the gate on the $1D$ transport. The quantum critical point is expected in the lowest energy scale.

There are several mechanisms for the gap formation, such as spontaneous dimerisation[7,39] and frustrating interactions[44–47] that are intriguingly governed by the Oshikawa-Yamanaka-Affleck criterion.[47] In our device, the exact origin of the plateaus is unclear and is far beyond our mean-filed analysis, but we can think about the band degeneracies in the valence band of Si are a possible origin. These extra degrees of freedom complicate the interactions among holes belonging to the different sub-bands with different effective masses. The formation of a local pseudo-spin singlet state among the valleys of sub-bands valleys and/or true degrees of freedom in the spin to form a magnetic singlet might also be related to the origin of the plateaus.

4.4 Phase Diagrams

The $I_{\rm d} - V_{\rm d}$ characteristics, drain transconductance ($g_{\rm d} = \partial I_{\rm d}/\partial V_{\rm d}$), and gate transconductance ($g_{\rm g} = \partial I_{\rm d}/\partial V_{\rm g}$) are shown in Figs. 9 and 17. No anomalies were observed at temperatures higher than 30 K, and the field-induced phase transition was observed below 25 K. The qualitative features of the $I_{\rm d} - V_{\rm d}$ curves were successfully simulated (Fig. 13). We can

clearly identify the phase boundaries between the classical and quantum transport regimes in $g_{\rm d}$ and $g_{\rm g}$ (Fig. 17). At lower temperatures, we can identify the AF-electric phase and the plateau regime in $g_{\rm d}$, but there is no negative differential conductance in $g_{\rm g}$. This observation indicates that high E_y at a higher carrier density is needed to generate the AF-electric phase, while $I_{\rm d}$ always increases upon increasing of the hole concentrations by $V_{\rm g}$. The phase boundaries for the quantum transport decreased within the $V_{\rm d} - V_{\rm g}$ planes as we decreased the temperature (Fig. 9), and the AF-electric regime was expanded (Fig. 17). This is consistent with the renormalisation group flow (Fig. 16 (b)),[7,38,67] and thus, the TLL behaviour is expected at the boundary of the ferroelectric phase at lower temperatures (Fig. 17 (b) at 5 K). We could not determine a clear quantum phase transition between the AF-electric, XY, and ferroelectric phases, presumably because the quantum critical point and the renormalisation fixed line exist at zero temperature,[7] and quantum critical behaviour can only be observed at finite temperatures.[58] In our system, there exists intrinsic disorders due to random dopant configurations unequal lattice spacing. Impacts of disorders are discussed in Appendix D.

4.5 Impacts of magnetic fields

To identify the internal magnetic structure of the quantum dipole, we have also applied high magnetic fields at 5 K (Fig. 18). This experiment was inspired by the Meissner effect and a breakdown of superconductivity under the applications of high magnetic fields.[1,2,7,74–76] In a superconductor, Cooper pairs form local singlets, which will be broken if the applied magnetic field is sufficiently high. Depending on the types of superconductivity, the breakdown may accompany the first order phase transition (type-I) or it may generate the intermediate phase (type-II), in which the magnetic domains with flux vortices are formed. The latter is especially interesting at lower dimensions since the Berezinskii-Kosterlitz-Thouless (BKT) transition,[65–67] which is characterised by an infinite order phase transition with a universal jump in the order parameter at the transition, is expected due to the paring of the vortex and anti-vortex.

Fig. 18 shows our experimental results. We could not identify clear changes upon the applications of magnetic fields up to 12 T. This indicates that we could not substantially impact the origin of the transport anomalies. The result implies that the magnetic structure of the quantum dipole does not have a major effect on the transport, but further investigations are needed to determine the exact internal structure of the quantum dipole.

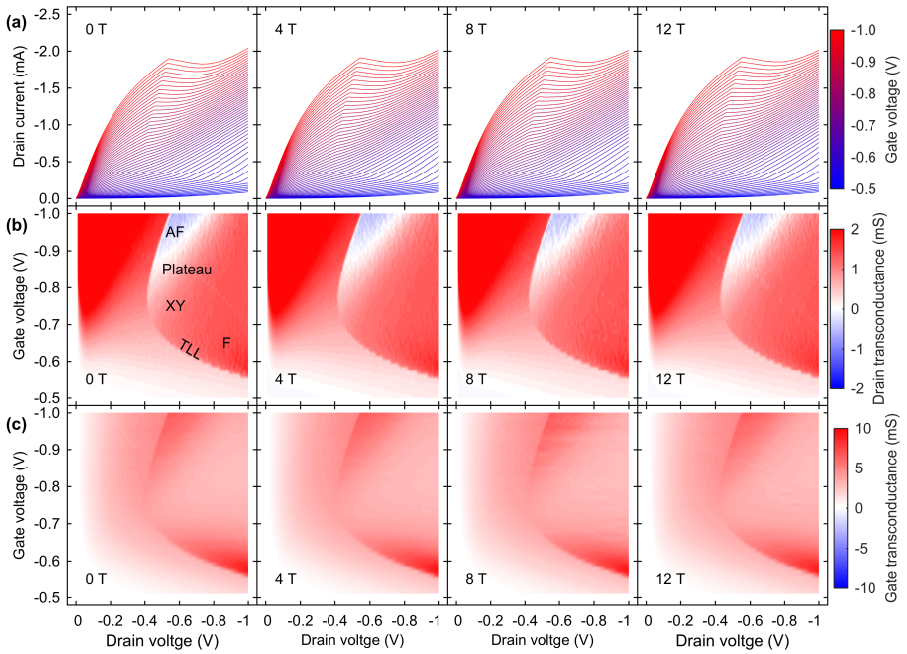

Fig. 18. (Color) Phase diagrams of the 1D channel under various magnetic fields at 5K. The panels of the figure show the results of the application of the magnetic fields of 0, 4, 8, and 12 T, respectively. (a) Transitions in the transport properties. (b) Drain transconductance, which shows the impacts of transverse electric fields. (c) Gate transconductance, which shows the doping effects.

4.6 Impacts of body bias on phase diagrams

According to the renormalisation flow[7,38,67] (Fig. 16 (b)), to see the antiferroelectric phase more clearly, we should reduce the energy scale of the system and increase E_z (or J^z). Following the theoretical predictions, we have reduced temperatures down to 5 K and obtained phase diagrams under the applications of the forward body bias (V_b) to the *n*-well, which reduced the threshold voltage of the transistor to increase E_z (Fig. 19). As a result, the antiferroelectric phase, which has a negative g_d (the blue regions in Fig. 19 (b)), expanded substantially, as we reduced V_b. This means that we could successfully confirmed the body contact to observe the expected impacts of the body bias on stabilising the AF-electric phase under the application of stronger vertical electric fields (Fig. 19), which is consistent with the renormalisation group flow (Fig. 16 (b)). Therefore, the phase diagrams and the generic trends were consistent with theoretical predictions based on the XXZ model.[7,38,67]

4.7 Anomalous gate leakage currents

We also found an additional piece of evidence confirming the formation of quantum dipoles in I_g (Figs. 10 and 20). Usually, I_g has no or very weak temperature dependence due to

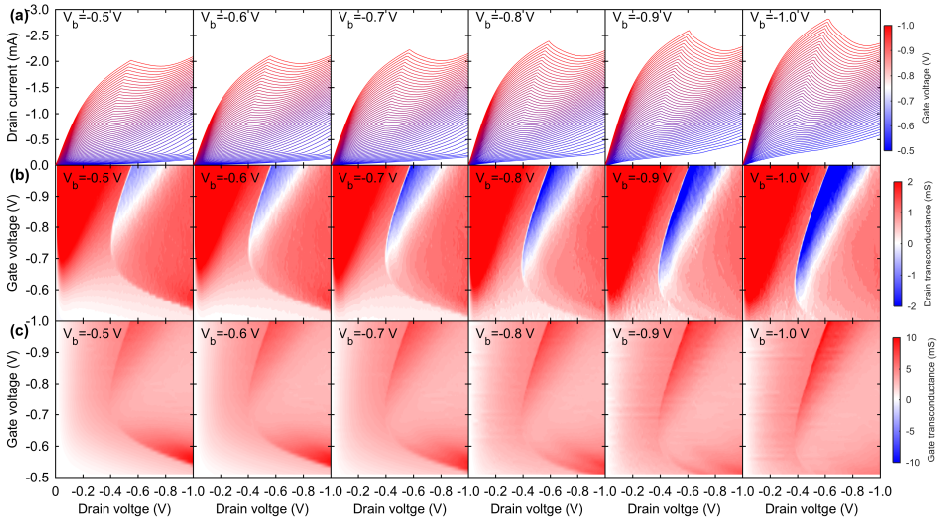

Fig. 19. (Color) Phase diagrams of the 1D channel under strong electric fields controlled by the body biasing. Measurements were made at 5K. (a) Transitions in the transport properties. (b) Drain transconductance, which shows the impacts of enhanced *vertical* electric fields. The antiferroelectric phase boundaries expanded as we increased the forward bias on $V_{\rm b}$ from -0.5 V to -1.0 V. (c) Gate transconductance, which shows the doping effects.

the intrinsic quantum nature of the direct tunnelling currents, which can be understood within the framework of the one-body Schrödinger equation.[2,9,74,75] On the other hand, many-body interactions among dipoles are necessary to understand the observed exponential increases in the tunnelling currents with decreasing temperatures. The local increase in the electric field perpendicular to the MOS interface, E^z, from the development of the local order parameter $\langle P_j^z \rangle$ must be considered. $I_{\rm g}$ exponentially increases with $V_{\rm g}$ (Fig. 20 (b)), which means the extra contributions to E_i^z from the molecular mean fields would significantly affect $I_{\rm g}$. This was especially true at lower temperatures and higher $V_{\rm g}$, where $\langle P_j^z \rangle$ develops. Another anomaly was observed in the $V_{\rm d}$ dependence (Fig. 20 (a)). As we reduced $V_{\rm d}$ from 0 V to -1 V at fixed $V_{\rm g}$, the voltage difference between $V_{\rm g}$ and $V_{\rm d}$ decreased; however, $I_{\rm g}$ exponentially increased, instead. This increase in the current with decreasing *external* electric field is quite unusual. The only way to explain this increase in $I_{\rm g}$ is based on the local increase in the *effective* electric field upon the development of $\langle P_j^z \rangle$. This is a firm evidence showing the quantum dipoles are controlling the quantum transport at low temperatures (Figs. 10 and 20). The enhancement of the resonant tunnelling was previously observed in a double layer quantum Hall ferromagnet.[85] The observed enhancement under the application of the low in-

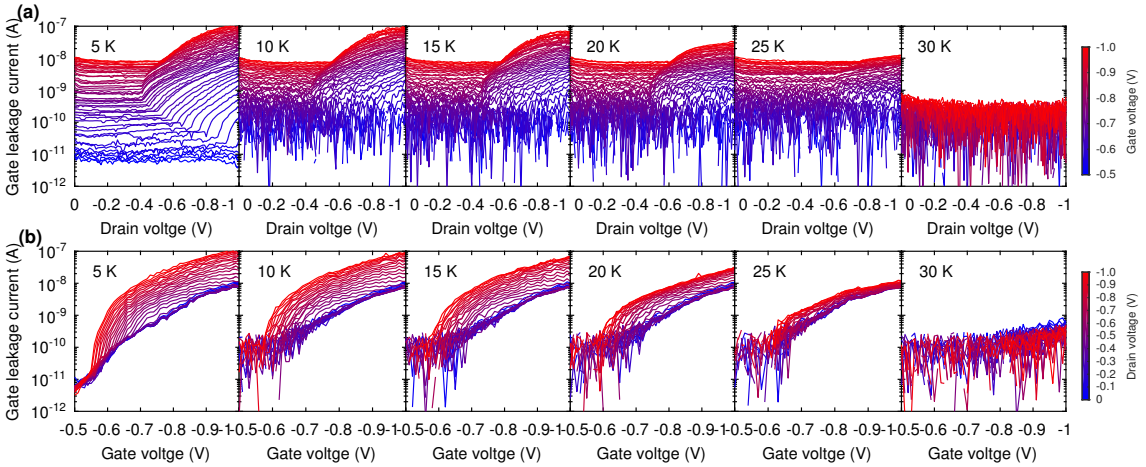

Fig. 20. (Color) Enhanced gate leakage current by quantum dipole formation after phase transition. (a) Field-induced phase transitions and exponential increases in the tunnelling currents at lower temperatures. V_g was held constant at -1 V. (b) Gate-induced phase transitions and exponential increases in the tunnelling currents as the order parameter of the quantum dipole developed. V_d was held constant at -1 V. The anomalous increase in the current was attributed to the increase in the local electric field due to the dipole order.

terlayer voltage has been reported to be a result of the collective excitaions of the Goldstone mode.[85] Our device may have some similarities to the bilayered quantum Hall systems[3,85] and coupled quantum wires,[86,87] in which the interactions between excitons are important. In our device, electrons and holes are physically separated by the gate insulator, and a similar separation is expected in a coupled quantum wires.[86,87] The physical separation was also controlled by a double quantum well heterostructure.[85] One notable difference in our system is the indirect band gap nature of Si, which makes it more difficult to investigate by excitonic recombination processes due to the inefficient light emissions; however, the long life time may help to expect the correlated many-body effects. Addressing the dynamics of the dipoles in our device is beyond the scope of this paper, but researchers working on excitions will be able to investigate the dynamics in time resolved experiments in the future. Another difference of our device relative to III-V systems is the cleanliness of the channel. In our *p*-channel MOSFET, B impurities are heavily doped up to 10^{20} cm^{-3} because the solid solubility of impurities in this system is orders of magnitude higher than it is in III-V materials.[9] Therefore, the poly-Si gate electrode is dirty, and we expect the short mean-free path to be approximately 10 nm. At low T, these impurities will strongly trap the quantum dipoles due to the Anderson localisation[30,88] and these dipoles cannot move freely. On the other hand, the channels of III-V materials are much cleaner, and thus ballistic transport would be expected at low T and excitons can move freely. To the best of our knowledge, transport properties

of III-V materials that are similar to what we observed in our materials have not been reported. These differences between Si and III-V materials might be the cause of the observed anomalous transport properties.

4.8 Similarity to phase diagrams of cuprates

We also generated phase diagrams against temperature, $V_{\rm d}$, and $V_{\rm g}$ (Fig. 21). The significant advantage of our system compared with other strongly correlated electron systems is the ability to control the phases solely by changing the voltages. We found that the transition temperature depends on the applied field condition (Fig. 21), and both antiferroelectric and ferroelectric phases were stabilised at $V_{\rm d} = -0.6$ V (Fig. 21 (b)) . In particular, the phase diagram upon changing the carrier density at $V_{\rm d} = -0.6$ V (Fig. 21 (b)) resembles the phase diagram of high-$T_{\rm c}$ superconducting cuprates.[6)] This can be understood by the mapping of the repulsive Hubbard model to the attractive Hubbard model under a magnetic field by the particle-hole transformation of one spin (up or down).[7,82)] In this respect, quantum antiferroelectric (CDW) and ferroelectric (BEC) phases in our device would correspond to the antiferromagnetic Mott insulator and d-wave superconductivity in cuprates.[6)] The transport dynamics in $1D$ is also ultimately linked to a $2D$ system, since a quantum system of $1D$ space-time is equivalently mapped to the corresponding statistical system of $2D$ space at a finite temperature.[7)] Furthermore, the current plateau would be relevant to the pseudo-gap phase,[6)] which is considered to be crucial to understand the mechanism of the high-$T_{\rm c}$ superconductivity. It was quite surprising for us to see a quantum ferroelectric state, which is equivalent to the exciton BEC, at relatively high transition temperature of 25 K, but physics responsible for the phase would be correlated to the similar mechanism in high-$T_{\rm c}$ cuprates. The recoveries of Fermi liquid behaviours[6)] at doping concentrations far away from $n = 1$ are also similar to our classical transport at lower gate-induced doping. We also observed the re-entrant nature of the phase transitions towards the emergence of the plateau regime at $V_{\rm d} = -0.5$ V (Fig. 21 (b)), which corresponds to the magnetisation plateau[7,39,42,44–47)] in the half spin magnetic models.

5. Conclusion

We discovered a novel transport property of a Si MOS field-effect transistor that has a wide and short p-channel at low temperatures. Anomalies were found after the pinch-off of the channel where $1D$ quantum dipoles were formed at the source edge of the channel. We found three important regimes; a quantum antiferroelectric phase, pseudo-gap phase, and

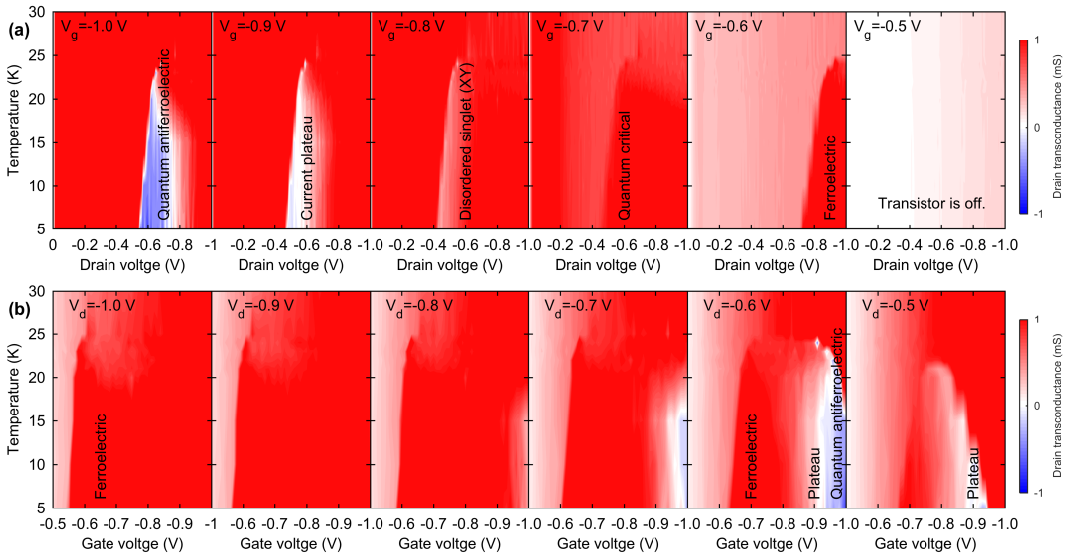

Fig. 21. (Color) Temperature-fields phase diagrams of the 1D channel at L =55 nm. (a) Field-induced phases. The quantum dipoles were aligned by strong transverse electric fields. (b) Transitions of anomalous transport states by carrier doping. The quantum antiferroelectric state was realised near half-filling, while the ferroelectric state was realised at lower doping. The plateau regime was found in between the antiferroelectric and ferroelectric states and corresponds to the pseudo-gap phase.

ferroelectric phase, which exhibit negative differential conductance, plateaus, and increases in the drain currents due to the condensations of excitons, respectively. The qualitative features of our device can be explained by an XXZ Heisenberg antiferroelectric quantum dipole model in conjunction with known theoretical models. Considering the impressive tunability of the electronic states by high electric fields, quantum dipole systems using conventional Si transistors will offer a new platform for investigating $1D$ strongly correlated systems. Our experimental results suggest that the scaling of Si technologies is opening up a new era for a quantum regime after a phase transition from a classical regime.

Acknowledgments

This work is supported by the EPSRC Manufacturing Fellowship (EP/M008975/1), EU FP7 Marie-Curie Career-Integration-Grant (PCIG13-GA-2013-618116), the University of Southampton Zepler Institute Research Collaboration Stimulus Fund, the EMPIR programme co-financed by the Participating States, and from the European Union ' s Horizon 2020 research and innovation programme. We would like to thank our colleagues, managers, and our clean room engineers for their support in fabricating our device. S.S. would like to express his

626 sincere thanks to Dr T Onai, Dr T Arai, Dr H Fukuda, Dr K Torii, Dr D Williams, Prof S Oda,
627 Prof H Mizuta, and Prof N Koshida for their substantial support in achieving a Mott transistor
628 through JST CREST, SORST, and industrial funding programs. The data from the paper can
629 be obtained from the University of Southampton ePrint research repository: http://dx.doi.org/
630 10.5258/SOTON/405381.

631 Appendix A: Technical Terms

632 Considering interdisciplinary nature of this research, we provide the list of abbreviations
633 and variables in Table A-1.

Table A·1.: List of abbreviations and variables.

Name	Symbol
Annihilation operator for the conduction band	$b_{\mathbf{k}c}$
Annihilation operator for the depletion charge	$c_{\mathbf{k}\uparrow}$
Annihilation operator for the valence band	$b_{\mathbf{k}v}$
Annihilation operator for the valence band hole	$c_{\mathbf{k}\downarrow}$
Anti-Ferro	AF
Attractive interaction	U
Average area of the lattice site	$S = a^2$
Average dipole moment along x	$\langle P^x \rangle$
Average dipole moment along y	$\langle P^y \rangle$
Average dipole moment along z	$\langle P^z \rangle$
Average distance between boron atoms	a
Average exchange energy	J
Average filling for pseudo spin σ	n_σ
Average filling fraction	$n = n_\uparrow + n_\downarrow$
Average random z-field	$\langle \Delta E_z^i \rangle$
Axis along the source-to-drain direction	x
Axis along the gate	y
Axis perpendicular to the substrate	z
Berezinskii-Kosterlitz-Thouless	BKT
Bose-Einstein condensation	BEC
Charge-Density-Waves	CDWs
Channel length	L

Name	Symbol
Channel width	W
Complementary Metal-Oxide-Semiconductor	CMOS
Conduction band	ϵ_{c}
Correlation length	ξ
Creation operator for the conduction band electron	$b^{\dagger}_{\mathbf{k}\mathrm{c}}$
Creation operator for the depletion charge	$c^{\dagger}_{\mathbf{k}\uparrow}$
Creation operator for the valence band electron	$b^{\dagger}_{\mathbf{k}\mathrm{v}}$
Creation operator for the valence band hole	$c^{\dagger}_{\mathbf{k}\downarrow}$
Chemical potential for electrons	μ_{n}
Chemical potential for the gate electrode	μ_{g}
Chemical potential for holes	μ_{h}
Coupling constant	G
Critical temperature	T_{c}
Critical drain voltage at the kink	V_{c}
Critical electric field for the pinch off	E_{c}
Destruction operator for the conduction band electron	$b_{\mathbf{k}\mathrm{c}}$
Destruction operator for the depletion charge	$c_{\mathbf{k}\uparrow}$
Destruction operator for the valence band electron	$b_{\mathbf{k}\mathrm{v}}$
Destruction operator for the valence band hole	$c_{\mathbf{k}\downarrow}$
Drift velocity	v_y
Dielectric constant in the vacuum	ϵ_0
Dirac's constant	$\hbar$
Drain current	I_{d}
Drain transconductance	$g_{\mathrm{d}} = \partial I_{\mathrm{d}}/\partial V_{\mathrm{d}}$
Drain voltage	V_{d}
Effective electric field by the chemical potential	E_z^{chem}
Effective electric mean-field along y	E^{y}_{MF}
Effective mass	m^*
Effective mobility	μ_{eff}
Effective oxide thickness due to quantum confinement	t_{QM}
Elementary charge	e
Electric field of the quantum dipole model along x	E_x
Electric field of the quantum dipole model along y	E_y

Name	Symbol
Electric field of the quantum dipole model along z	E_z
Energy level for boron	E_B
Energy for classical mechanical MOS model	E_{CM}
Equivalent Oxide Thickness (EOT)	t_{ox}
Exchange interaction	J
Exchange interaction in the xy-plane	J^{xy}
Exchange interaction along z	J^z
External electric field along x	E_x^{ext}
External electric field along y	E_y^{ext}
External electric field along z	E_z^{ext}
Field-Effect-Transistor	FET
Gate oxide capacitance	C_{ox}
Gate transconductance	$g_{\mathrm{g}} = \partial I_{\mathrm{d}}/\partial V_{\mathrm{g}}$
Gate voltage	V_{g}
Hamiltonian for external fields	H_{ext}
Hamiltonian for gate	H_{gate}
Hamiltonian for interaction energy	H_{int}
Hamiltonian for kinetic energy	H_{kin}
Hamiltonian for quantum XXZ model	H
Hamiltonian for randomness	H_{Random}
Hamiltonian for random z-field	H_{ZF}
Hamiltonian for random planer exchange	H_{PE}
Hamiltonian for random z-z exchange	H_{ZE}
Hamiltonian for substrate	H_{sub}
Information Communications Technologies	ICT
i-th lattice site	i
j-th lattice site	j
Length scale for renormalization	l
Levi-Civita fully antisymmetric tensor	$\epsilon_{\alpha\beta\gamma}$
Local dipole moment	$d_i = et_{\mathrm{ox}}^i$
Local gate oxide thickness	t_{ox}^i
Local lattice spacing	a_i
Local quantum capacitance	$C_{\mathrm{Q}}^i = C_{\mathrm{ox}} a_i^2$

Name	Symbol
Local variation of gate oxide thickness	$\Delta t^i_{\rm ox}$
Local variation of lattice spacing	Δa_i
Luttinger parameter	K
Mean squared random field strength	$D = \langle(\Delta E^i_z)^2\rangle$
Metal-Oxide-Semiconductor	MOS
Metal-Oxide-Semiconductor Field-Effect-Transistor	MOSFET
Nearest neighbour transfer energy for the gate	$t_\uparrow$
Nearest neighbour transfer energy for the substrate	$t_\downarrow$
Number operator at the i-th site	n_i
Number of the lattice sites	$N_{\rm L}$
One-dimensional	$1D$
Polarisation operator along x	P^x_i
Polarisation operator along y	P^y_i
Polarisation operator along z	P^z_i
Pseudo down spin for the gate	$\downarrow$
Pseudo up spin for the gate	$\uparrow$
Pseudo spin	σ
Quantum bit	Qubit
Quantum capacitance of the dipole	$C_{\rm Q} = C_{\rm ox}S$
Quantum dipole moment	$d = et_{\rm ox}$
Random planer exchange interaction	ΔJ^{xy}_{ij}
Random z-field	ΔE^i_z
Random z-z exchange interaction	ΔJ^z_{ij}
Relative dielectric constant of Si	$\kappa_{\rm Si} = 11.7$
Relative dielectric constant of SiO_2	$\kappa_{\rm SiO_2} = 3.9$
Saturation velocity	$v_{\rm sat}$
Silicon	Si
Silicon-oxynitride	SiON
Temperature	T
Threshold voltage	$V_{\rm t}$
Tomonaga-Luttinger Liquid	TLL
Transfer energy	$t_{ij\sigma}$
Two-dimensional	$2D$

Name	Symbol
Valence band	$\epsilon_{\rm v}$
Valence band edge	$E_{\rm v}$
Wavevector	$\mathbf{k}$

Appendix B: Attempt to Explain Experiments by Bloch Oscillations

We have considered Bloch oscillations as one of possible scenarios to explain these phenomena. The accelerated carriers can oscillate within a band under a constant applied electric field, which might explain the negative differential conductance.

To begin with, we calculate the mobility μ and the source-drain current $I_{\rm d}$ when Bloch oscillation is included. Following Esaki and Tsu,[77] we first calculate the mobility μ with semiclassical equations

$$\hbar\frac{dk}{dt} = eE, \tag{B·1}$$

$$\frac{dv}{dt} = \frac{1}{\hbar^2}\frac{d^2\varepsilon_k}{dk^2}eE, \tag{B·2}$$

where k and v are the carrier wavenumber and velocity in its 1D propagation direction, respectively, including a time (t) dependence, E is the electric field applied between the source and the drain, ε_k is the carrier energy dispersion, $\hbar$ is Planck's constant h divided by 2π, and e is the electric charge. For simplicity, we employ the energy dispersion defined in one dimension: $\varepsilon_k = \tilde{W}(1-\cos ka)/2$, where $\tilde{W}$ is the band width, which is related to the carrier effective mass m as $\tilde{W} = 2\hbar^2/(ma^2)$, where a is the Si lattice constant. Integration of Eq. (B·1) with t for a constant E gives $k = eEt/\hbar$, where the integration constant is set to be zero at $t = 0$.

The drift velocity $v_{\rm d}$ of the carriers is then given by

$$v_{\rm d} = \int_0^\infty \frac{dv}{dt}\, e^{-\frac{t}{\tau}}\, dt, \tag{B·3}$$

where it is defined as the carrier acceleration dv/dt multiplied by a damping factor $e^{-t/\tau}$ with an integration from $t = 0$ to ∞. This definition contains the relaxation of the carrier acceleration due to carrier scattering within a time τ to the dissipative environment.[89]

Inserting Eq. (B·2) with ε_k and k defined above into Eq. (B·3) and using the definition of the mobility μ (i.e., $v_{\rm d} = \mu E$), we obtain

$$\begin{aligned} v_{\rm d} &= \int_0^\infty \frac{1}{\hbar^2}\frac{d^2\varepsilon_k}{dk^2}\, eE\, e^{-\frac{t}{\tau}}\, dt \\ &= \frac{\tilde{W}a^2}{2\hbar^2}eE\int_0^\infty \cos(ka)\, e^{-\frac{t}{\tau}}\, dt \end{aligned}$$

$$= \frac{eE}{m}\int_0^\infty \cos\left(\frac{eEt}{\hbar}a\right) e^{-\frac{t}{\tau}}\, dt$$
$$= \mu E, \tag{B·4}$$

where

$$\mu = \frac{e\hbar^2}{m\tau}\frac{1}{(eEa)^2 + (\hbar/\tau)^2}. \tag{B·5}$$

Note that it has been shown that another derivation using the Boltzmann transport equation gives the same result as in Eqs. (B·4) and (B·5).[78,79)]

Next, we calculate the source-drain current I_d using Eq. (B·5). The source-drain current I_d at a low source-drain electric field is given by

$$I_\mathrm{d} = C_\mathrm{ox}(V_\mathrm{g} - V_\mathrm{th})Wv_\mathrm{d}$$
$$= \mu C_\mathrm{ox}(V_\mathrm{g} - V_\mathrm{th})WE, \tag{B·6}$$

where C_ox is the capacitance per gate area, V_g is the gate voltage, V_th is the threshold voltage, and W is the channel width. With the source-drain voltage V_d and the channel length L, the source-drain electric field E is of the form: $E = V_\mathrm{d}/L$. Substituting Eq. (B·5) for Eq. (B·6), we get

$$I_\mathrm{d} = \frac{e\hbar^2}{m\tau L}\frac{C_\mathrm{ox}(V_\mathrm{g} - V_\mathrm{th})WV_\mathrm{d}}{(eV_\mathrm{d}\,a/L)^2 + (\hbar/\tau)^2}, \tag{B·7}$$

where $E = V_\mathrm{d}/L$ was used. In Fig. B-1, we show Eq. (B·7) as a function of V_d, where $V_\mathrm{d}^\mathrm{Peak} = \hbar L/(e\tau a)$ is a voltage that gives a peak current $I_\mathrm{d}^\mathrm{Peak}$. To determine the numerical value of $V_\mathrm{d}^\mathrm{Peak} = \hbar L/(e\tau a)$, we insert $\hbar = 1.055 \times 10^{-34}$ J · s, $L = 55$ nm, $e = 1.602 \times 10^{-19}$ C, and $a = 0.543$ nm. As for τ, since it fluctuates from 0.1 ps to $\sim$ 1 ps, depending on experimental conditions,[90–92)] we use an intermediate value 0.5 ps. We then obtain $V_\mathrm{d}^\mathrm{Peak} = 0.13$ V. This value is smaller than $V_\mathrm{d}^\mathrm{Peak} \approx 0.4$ - 0.6 V observed in the experiment. Owing to the uncertainty in the value of τ, it could fit the experimental value.

As seen in Fig. B-1, at V_d higher than $V_\mathrm{d}^\mathrm{Peak}$, I_d decreases with V_d, which exhibits a negative differential conductance. This may partially explain the observed negative differential conductance in Fig. 15 (a). However, the experimental results show clear kinks, which might be the on-set of Bloch oscillation, while we cannot explain the threshold characteristics to start the Bloch oscillation. Another difficulty is the V_g dependence of the currents. We cannot explain the plateau (Fig. 15 (b)) nor the increase of the slope in I_d (Fig. 15 (c)). Moreover, we cannot explain the observed change upon changing temperatures. Essentially, Bloch oscillation is based on one-body free-particle motion, and it does not drastically change the transport properties. Therefore, the theoretical model must be developed further in order to understand

our experimental results.

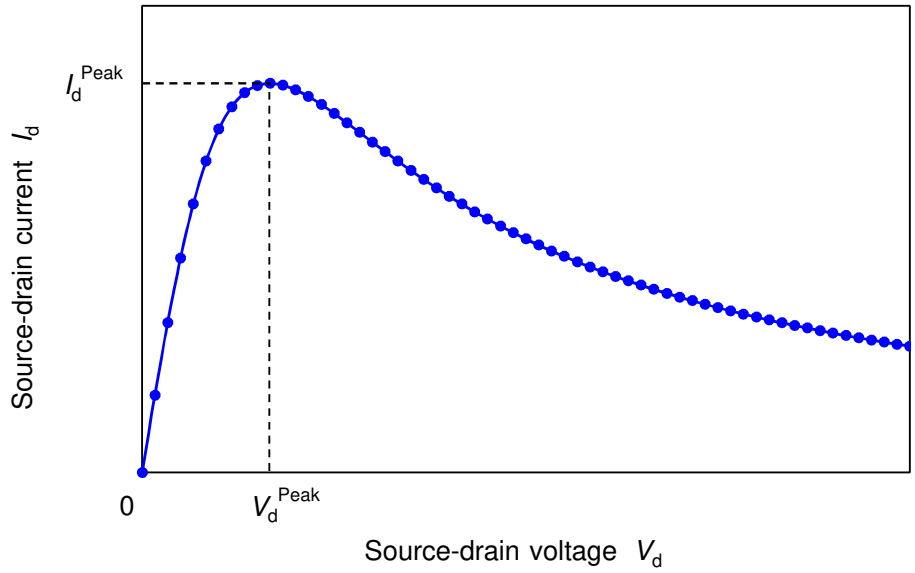

Fig. B·1. (Color) Calculated drain current I_d vs drain voltage V_d. There is a peak at $V_d^{Peak} = \hbar L/(e\tau a)$, which gives a current $I_d^{Peak} = (\hbar/2ma)C_{ox}(V_g - V_{th})W$.

Appendix C: Estimation of energy scales

The average lattice constant (a) of our quantum dipole model was estimated from the average distance between depletion charges (boron) in the polycrystalline-Si gate, whose carrier concentration was $N_g \sim 1 \times 10^{20}$ cm^{-3}, and it was found to be $a = N_g^{-1/3} \sim 2.2$ nm, which was comparable to t_{ox}. Assuming $S = a^2$, we estimated the attractive interaction, $U = e^2/(2C_Q) = e^2/(2C_{ox}S) \sim 1.2$ eV. The areal density of the dipole was $1/a^2 = N_g^{2/3} \sim 2.2\times10^{13}$ cm^{-2}. At $V_g = -1$ V, the hole density was $n_h \sim C_{ox}V_g/(-e) = 8.9 \times 10^{12}$ cm^{-2}, which was slightly less than the half filling ($n = 1$). If we estimate the transfer energy, t_σ, from the Fermi energy at $n_h = 5 \times 10^{12}$ cm^{-2}, assuming typical density of states,[9,23] we obtain $t_\uparrow \sim t_\downarrow \sim 29$ meV. Then, the exchange energy was estimated to be approximately $4t_\sigma^2/U = 2.8$ meV (33 K), which was comparable to the transition temperature (25 K). In the simulation, we assumed a slightly larger value of $J = 7$ meV with a number of the nearest neighbour sites of $z = 4$. This is coming from the overestimation of the transition temperature within the mean field theory.

When we applied the high E_y along the drain, we found a field-induced phase transition, and there is no anomaly in the transport properties at low E_y. We believe that the high horizontal electric field enhanced the quantum nature of the dipole.[93] This can be understood based on the finite life time, τ, of the dipole due to various scatterings in the channel. If E_y is

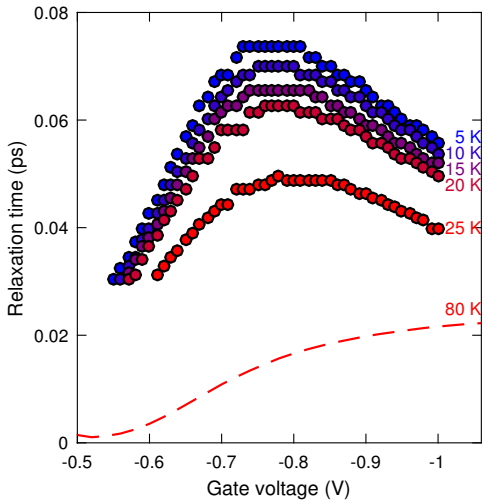

Fig. C·1. (Color) Lifetime of quantum dipoles extracted from the experimental transport data in a *p*-MOSFET. The extracted lifetime of a quantum dipole is shown as a function of the gate voltage at low temperatures. The dotted line shows the relaxation time estimated from the mobility at 80K. The lifetime is limited by Coulomb interactions at low carrier concentrations, and it is limited by surface roughness scattering at high vertical fields.

not sufficiently high, the dipole cannot be aligned to the y direction, and our description using dipoles will not be justified.

To predict the field-induced phase transition for the dipole ordering, $V_{\rm d}$ must be larger the critical voltage $V_{\rm c}$, which is the drain voltage at the anomaly seen in Fig. 9, to overcome the damping coming from the finite relaxation lifetime, τ, of the dipole. Therefore, quantum dipoles will become well-defined excitations, only when the expectation value, $\langle P^y \rangle$, is sufficiently large

$$\langle P^y \rangle E^y > e t_{\rm ox} V_{\rm c} / 2L = \hbar / \tau, \tag{C·1}$$

compared with the damping. The estimated τ from the experimentally obtained $V_{\rm c}$ is shown in Fig. C-1, and it was comparable to the relaxation time measured from the mobility measurement[94] at 80 K. Therefore, we required a critical drain voltage $V_{\rm c}$ to overcome the damping, and τ was estimated to be around $0.03 - 0.07$ ps, which is consistent with the relaxation time, estimated from the mobility (Fig. C-1).

Appendix D: Impacts of random dopant fluctuations and variations in the gate oxide thickness

So far, we have discussed our experimental data using a very simplified toy model, that assumes a perfect periodic superlattice made of impurities. Obviously, this is idealised and is far from the realistic experimental situation, in which dopants are randomly distributed[7,95–98] and the gate oxide thickness varies locally due to the surface roughness[23,99] on the atomic scale. In fact, it is well known that the impact of disorders due to the Anderson localisation is stronger in lower dimensional systems and especially in a $1D$ system.[88] In the quantum XXZ spin models, the impacts of random magnetic fields and random exchange interactions were theoretically investigated in detail.[7,95–98] Theoretically, random magnetic fields significantly changed the long-range order of the phase diagram, while Ising orders were robust against random exchange interactions by the renormalisation group theory.[95] In this section, we discuss about the impacts of randomness on our device.

In our p-MOSFET, the B impurities are randomly distributed in the gate electrode, and the locations of the impurities define the lattice sites, i, for the quantum XXZ dipole model. Therefore, the lattice spacing, a_i, is not constant at all and depends on the location, i. Another important variations in a MOSFET are the local thickness variations of the gate oxide thickness due to the roughness at the Si surface[23] as well as the remote-surface-roughness at the gate electrode.[99] Local roughness on the order of 0.2 nm is considered to be inevitable,[23,99] and therefore, we must consider the dependence of the local gate oxide thickness, $t^i_{\rm ox}$, dependence on i, which results in the local variation of the dipole moment, $d_i = et^i_{\rm ox}$. B impurities are also randomly distributed along the vertical direction, z, perpendicular to the MOS interface, which also adds to the variation in d_i.

Therefore, to take these variations into account, we must consider

$$a \quad \rightarrow \quad a_i = a + \Delta a_i \tag{D·1}$$

$$t_{\rm ox} \quad \rightarrow \quad t^i_{\rm ox} = t_{\rm ox} + \Delta t^i_{\rm ox}, \tag{D·2}$$

where Δa_i and $\Delta t^i_{\rm ox}$ are the local variations of the lattice spacing and gate oxide thickness, respectively. Then, the starting Hamiltonian must be modified to be

$$H_{\rm kin} + H_{\rm int} + H_{\rm ext} = -\sum_{ij\sigma} t_{ij\sigma} c^\dagger_{i\sigma} c_{j\sigma} - \mu \sum_{i\sigma} n_{i\sigma} - \sum_i U_i n_{i\uparrow} n_{i\downarrow} - E^{\rm ext}_y \sum_i P^y_i - \sum_i E^{\rm ext}_{i,z} P^z_i, \tag{D·3}$$

where the local Coulomb attractive interaction, U_i, and the local vertical external field, $E^{\rm ext}_{i,z}$,

depend on i. Here, the dipole operators must also be *redefined* as

$$P_i^x = \frac{d_i}{2}(c_{i\uparrow}^\dagger c_{i\downarrow}^\dagger + c_{i\downarrow}c_{i\uparrow}) \tag{D·4}$$

$$P_i^y = \frac{d_i}{2i}(c_{i\uparrow}^\dagger c_{i\downarrow}^\dagger - c_{i\downarrow}c_{i\uparrow}) \tag{D·5}$$

$$P_i^z = \frac{d_i}{2}(n_{i\uparrow} + n_{i\downarrow} - 1), \tag{D·6}$$

where d_i is used instead of its average, d. The commutation relationship becomes

$$[P_i^\alpha, P_i^\beta] = id_i\epsilon_{\alpha\beta\gamma}P_i^\gamma. \tag{D·7}$$

U_i and $E_{i,z}^{\rm ext}$ are given by

$$U_i = \frac{e^2}{2C_{\rm Q}^i} \tag{D·8}$$

$$E_{i,z}^{\rm ext} = -\frac{V_{\rm g} - V_{\rm t}}{t_{\rm ox}^i}, \tag{D·9}$$

where $C_{\rm Q}^i = C_{\rm ox}a_i^2$ is the local quantum capacitance. Experimentally, both variations of $\Delta t_{\rm ox}^i/t_{\rm ox}$ and $\Delta a_i/a$ are expected to be less than 10 %, since we would be able to identify significant device degradations in mobility and other parameters,[9,23,99] if there were significant variations. Thus, the Hamiltonian can be expanded in series by assuming these variations are small. The leading order perturbation of randomness to the Hamiltonian is given by

$$H_{\rm Random} = H_{\rm ZF} + H_{\rm PE} + H_{\rm ZE}, \tag{D·10}$$

where $H_{\rm ZF}$, $H_{\rm PE}$, and $H_{\rm ZE}$ are random z-field, random planer exchange, and random z-z exchange contributions,[95] respectively. We can thus obtain

$$H_{\rm ZF} = -\sum_i \Delta E_z^i P_i^z \tag{D·11}$$

$$H_{\rm PE} = \sum_{\langle ij\rangle} \Delta J_{ij}^{xy}(P_i^x P_j^x + P_i^y P_j^y) \tag{D·12}$$

$$H_{\rm ZE} = \sum_{\langle ij\rangle} \Delta J_{ij}^z P_i^z P_j^z, \tag{D·13}$$

where the random z-field, ΔE_z^i, and the planer exchange interaction, ΔJ_{ij}^{xy}, and the z-z exchange interaction, ΔJ_{ij}^z are given by

$$\Delta E_z^i = \frac{2}{d}\left(-\mu\frac{\Delta t_{\rm ox}^i}{t_{\rm ox}} + Un\frac{\Delta a_i}{a}\right) \tag{D·14}$$

$$\Delta J_{ij}^{xy} = J^{xy}\left(2\frac{\Delta a_i}{a} - 3\frac{\Delta t_{\rm ox}^i}{t_{\rm ox}}\right) \tag{D·15}$$

$$\Delta J^z_{ij} = J^z\left(2\frac{\Delta a_i}{a} - 3\frac{\Delta t^i_{\rm ox}}{t_{\rm ox}}\right). \quad \text{(D·16)}$$

Among these contributions, $H_{\rm ZF}$ is the most important, since even a small amount of disorders will destroy the long-range Ising orders according to the renormalisation group theory.[95] No matter how small the ΔE^i_z is, the effect is relevant on the Ising phases. Therefore, we cannot expect that the long range orders can survive under the random dopant fluctuations and the variations in the local gate oxide thickness.

However, this does not exclude short-range orders of dipoles that covers only a few impurity sites. In fact, according to the exact diagonalisation study of the XXZ model,[96] the correlation length, ξ, can be as large as $10a$ to $300a$, depending on the mean squared random field strength, $D = \langle(\Delta E^i_z)^2\rangle$, while the average random z-field is zero, $\langle\Delta E^i_z\rangle = 0$. This is enough long for us to predict the local effective molecular field, $E^y_{\rm MF}$ of Eq. (33), since the interaction is dominated by the dipoles at the nearest neighbours. In other words, the small domains of AF and ferroelectric orders will produce the transverse electric fields, which affect the drain currents. Therefore, true long-range orders are not required to understand the experimental data. ξ is expected to be especially large, when the ferroelectric anisotropy is large,[96] meaning that a larger domain size is expected for the ferroelectric ordered state.

On the other hand, ΔJ^{xy}_{ij} and ΔJ^z_{ij} are irrelevant for Ising orders.[95] Thus, the long-range ordered phases of AF and ferroelectric states exist, and there are phase boundaries between a random singlet phases. Therefore, in the absence of $H_{\rm ZF}$, we should expect quantum phase transitions between Ising ordered phases and the random singlet phases. Experimentally, there is no clear evidence of a quantum phase transition from changing $V_{\rm d}$ and $V_{\rm g}$. This is consistent with the above picture, that shows $H_{\rm ZF}$ is not negligible, and the long-range orders are destroyed. In the absence of the long-range order, we should observe a crossover among short-range ordered states of the AF, ferroelectric, and random singlet states. Therefore, we believe that the observed dipole orders are short-range in nature, and the random dopant fluctuations and local thickness variations substantially explain the observed crossover without a quantum phase transition.

Appendix E: Reproducibility of phase diagrams

We have also confirmed the reproducibility of the observed phase diagrams using a transistor with the different channel length (75 nm, Fig. E-1).

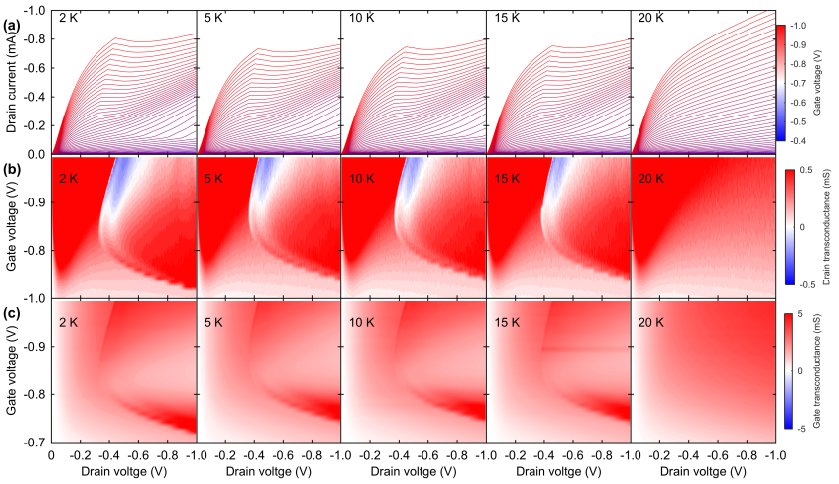

Fig. E·1. (Color) Phase diagrams of the 1D channel under strong electric fields. A p-channel MOSFET with L =75 nm and W =10 μm was used to evaluate the reproducibility of the results presented in the main text. (a) Transitions in the transport properties with changing temperatures. (b) Field-induced transitions probed by $g_{\rm d}$. (c) Impact of carrier doping by the gate on the 1D transport.

References

1) A. A. Abrikosov, L. P. Gorkov, and I. E. Dzyaloshinski: *Methods of Quantum Field Thoery in Statistical Physics* (Dover, 1975).

2) A. Altland and B. Simons: *Condensed Matter Field Theory* (Cambridge University Press, 2010).

3) Z. F. Ezawa: *Quantum Hall Effects: recent thoretical and experimental developments* (World Scientific, 2013).

4) C. D. Batista: Phys. Rev. Lett. **89** (2002) 166403.

5) T. Byrnes, N. Y. Kim, and Y. Yamamoto: Nat. Phys. **10** (2014) 803.

6) P. A. Lee, N. Nagaosa, and X. G. Wen: Rev. Mod. Phys. **78** (2006) 17.

7) T. Giamarchi: *Quantum Physics in One Dimension* (Oxford University Press, 2004).

8) J. Custers, P. Gegenwart, H. Wilhelm, K. Neumaler, Y. Tokiwa, O. Trovarelli, C. Geibel, F. Steglich, C. Pépin, and P. Coleman: Nature **424** (2003) 524.

9) Y. Taur and T. H. Ning: *Fundamentals of Modern VLSI Devices* (Cambridge University Press, 2013) 2nd ed.

10) T. Kadowaki and H. Nishimori: Phys. Rev. E **58** (1998) 5355.

11) I. M. Georgescu, S. Ashhab, and F. Nori: Rev. Mod. Phys. **86** (2014) 153.

12) K. Kasamatsu, I. Ichinose, and T. Matsui: Phys. Rev. Lett. **111** (2013) 115303.

13) Y. Nakamura, Y. A. Pashkin, and J. S. Tsai: Nature **398** (1999) 786.

14) M. W. Johnson, M. H. S. Amin, S. Gildert, T. Lanting, F. Hamze, N. Dickson, R.Harris, A. J. Berkley, J. Johansson, P. Bunyk, E. M. Chapple, C. Enderud, J. P. Hilton, K. Karimi, E. Ladizinsky, N. Ladizinsky, T. Oh, I. Perminov, C. Rich, M. C. Thom, E. Tolkacheva, C. J. S. Truncik, S. Uchaikin, J.Wang, B.Wilson, and G. Rose: Nature **473** (2011) 194.

15) I. Bloch, J. Dalibard, and S. Nascimbène: Nat. Phys. **8** (2012) 267.

16) A. Aspuru-Guzik and P. Walther: Nat. Phys. **8** (2012) 285.

17) M. J. Hartmann, F. G. S. L. Brandão, and M. B. Plenio: Laser & Photon. Rev. **2** (2008) 527.

18) S. Ma, B. Dakic, W. Naylor, A. Zeilinger, and P. Walther: Nat. Phys. **7** (2011) 399.

19) R. H. Hadfield: Nat. Photon. **3** (2009) 696.

20) D. Rotta, F. Sebastiano, E. Chrbon, and E. Prati: npj Quantum Information **3** (2017) 26.

807 21) B. Patra, R. M. Incandela, J. P. G. v. Dijk, H. A. R. Homulle, L. Song, M. Shahmo-
808 hammadi, R. B. Staszewsi, A. Vladimirescu, M. Babaie, F. Sebastiano, and E. Charbon:
809 IEEE J. Solid-State Circuits **99** (2017) 1.

810 22) B. E. Kane: Nature **393** (1998) 135.

811 23) T. Ando, A. B. Fowler, and F. Stern: Rev. Mod. Phys. **54** (1982) 437.

812 24) G. E. Moore: Electronics **38** (1965) 114.

813 25) G. D. Wilk, R. M. Wallace, and J. M. Anthony: J. Appl. Phys. **89** (2001) 5243.

814 26) M. L. Lee, E. A. Fitzgerald, M. T. Bulsara, M. T. Currie, and A. Lochtefeld: J. Appl.
815 Phys. **97** (2005) 011101.

816 27) D. Hisamoto, W. Lee, J. Kedzierski, H. Takeuchi, K. Asano, C. Kuo, E. Anderson,
817 T. King, J. Bokor, and C. Hu: IEEE Trans. Electron Devices **47** (2000) 2320.

818 28) R. P. Feynman: IEEE J. Microelectromechanical Systems **1** (1992 (The transcript of a
819 talk in 1959 at the annual meeting of the American Physical Society (APS))) 60.

820 29) K. v. Klitzing, G. Dorda, and M. Pepper: Phys. Rev. Lett. **45** (1980) 494.

821 30) P. W. Anderson: Phys. Rev **109** (1958) 1492.

822 31) R. B. Laughlin: Phys. Rev. B **23** (1981) 5632.

823 32) J. Gorman, D. G. Hasko, and D. A. Williams: Phys. Rev. Lett. **95** (2005) 090502.

824 33) X. Mi, J. V. Cady, D. M. Zajac, P. W. Deelman, and J. R. Petta: Science **10.1126** (2016)
825 science.aal2469.

826 34) F. A. Zwanenburg, A. S. Dzurak, A. Morello, M. Y. Simmons, L. C. L. Hollenberg,
827 G. Klimeck, S. Rogge, S. N. Coppersmith, and M. A. Eriksson: Rev. Mod. Phys. **85**
828 (2013) 961.

829 35) S. Tomonaga: Prog. Theor. Phys. **5** (1950) 544.

830 36) J. M. Luttinger: J. Math. Phys. **4** (1963) 1154.

831 37) E. H. Lieb and F. Y. Wu: Phys. Rev. Lett. **20** (1968) 1445.

832 38) K. G. Wilson: Rev. Mod. Phys. **47** (1975) 773.

833 39) F. D. Haldane: Phys. Rev. Lett. **45** (1980) 1358.

834 40) F. D. Haldane: Phys. Rev. B **25** (1982) 4925.

835 41) F. D. M. Haldane: Phys. Lett. A **93** (1983) 464.

836 42) I. Affleck: J. Phys.: Condens. Matter **1** (1989) 3047.

837 43) H. Tasaki: Phys. Rev. Lett. **66** (1991) 798.

838 44) K. Hida: J. Phys. Soc. Jpn. **63** (1994) 2359.

839 45) K. Okamoto: Solid State Commun. **98** (1996) 245.

840 46) M. Oshikawa and I. Affleck: Phys. Rev. Lett. **79** (1997) 2883.

841 47) M. Oshikawa, M. Yamanaka, and I. Affleck: Phys. Rev. Lett. **78** (1997) 1984.

842 48) S. Furukawa, M. Sato, S. Onoda, and A. Furusaki: Phys. Rev. B **86** (2012) 094417.

843 49) N. D. Mermin and H. Wagner: Phys. Rev. Lett. **17** (1966) 1133.

844 50) M. Bockrath, D. H. Cobden, J. Lu, A. G. Rinzler, R. E. Smalley, L. Balents, and P. L.
845 McEuen: Nature **397** (1999) 598.

846 51) Z. Yao, H. W. C. Posta, L. Balents, and C. Dekker: Nature **402** (1999) 273.

847 52) A. M. Chang: Rev. Mod. Phys. **75** (2003) 1449.

848 53) S. Jezouin, M. Albert, F. D. Parmentier, A. Anthore, U. Gennser, A. Cavanna, I. Safi,
849 and F. Pierre: Nat. Commun. **4** (2013) 1802.

850 54) M. Moreno, C. J. B. Ford, Y. Jin, J. P. Griffiths, I. Farrer, G. A. C. Jones, D. A. Ritche,
851 O. Tsyplyatyev, and A. J. Schofield: Nat. Commun. **7** (2016) 12784.

852 55) M. M. Mirza, F. J. Schupp, J. A. Mol, D. A. MacLaren, G. Andrew, D. Briggs, and D. J.
853 Paul: Sci. Rep. **7** (2017) 3004.

854 56) A. Einstein and J. Laub: Annalen der Physik **26** (1908) 532.

855 57) P. A. M. Dirac: Proc. Roy. Soc. A, Vol. 133, 1931, pp. 60–72.

856 58) M. Vojta: Rep. Prog. Phys. **66** (2003) 2069.

857 59) S. E. Rowley, J. S. L, R. P. Smith, M. D. M. P, M. Itoh, J. F. Scott, G. G. Lonzarich, and
858 S. Saxena: Nat. Phys. **10** (2014) 369.

859 60) J. Bardeen, L. N. Cooper, and J. R. Schrieffer: Phys. Rev. **108** (1957) 1175.

860 61) J. G. Bednorz and K. A. Müller: Z. Physik B - Condensed Matter **64** (1986) 189.

861 62) D. C. Tsui, H. L. Störmer, and A. C. Gossard: Phys. Rev. Lett. **48** (1982) 1559.

862 63) R. B. Laughlin: Phys. Rev. Lett. **50** (1983) 1395.

863 64) K. S. Novoselov, A. K. Geim, S. V. Morozov, D. Jiang, M. I. Katsnelson, I. V. Grigorieva,
864 S. V. Dubonos, and A. A. Firsov: Nature **438** (2005) 197.

865 65) V. L. Berezinskii: Soviet Phys. JETP **32** (1971) 493.

866 66) J. M. Kosterlitz and D. J. Thouless: J. Phys. C: Solid State Phys. **5** (1972) L124.

867 67) J. M. Kosterlitz: J. Phys. C: Solid State Phys. **7** (1974) 1046.

868 68) C. J. Glassbrenner and G. A. Slack: Phy. Rev. **134** (1964) A1058.

869 69) H. Hanamura, M. Aoki, T. Masuhara, O. Minato, Y. Sakai, and T. Hayashida: IEEE J.
870 Solid-State Circuits **21** (1986) 484.

871 70) K. L. Kasley, G. M. Oleszek, and R. L. Anderson: Solid-State Circuits **36** (1993) 945.

872 71) M. V. Fischetti and S. E. Laux: Int. Electron Devices Meeting, 1995, pp. 305–308.

873 72) A. Mercha, J. M. Rafi, E. Simoen, E. Augendre, and C. Claeys: IEEE Trans. Electron
874 Devices **50** (2003) 1675.

875 73) M. Casé, J. Pretet, S. Cristoloveanu, T. Poiroux, C. Fenouillet-Beranger, F. Fruleux,
876 C. Raynaud, and G. Reimbold: Solid State Electron. **48** (2004) 1243.

877 74) X. G. Wen: *Quantum Field Theory of Many-Body Systems* (Oxford University Press,
878 2004).

879 75) N. Nagaosa: *Quantum Field Theory in Condensed Matter Physics* (Springer, 1999).

880 76) L. P. Lévy: *Magnetism and Superconductivity* (Springer, 1997).

881 77) L. Esaki and R. Tsu: IBM J. Res. Dev. **14** (1970) 61.

882 78) F. Meng: Ph.D. Thesis, Universite Paris-Sud XI, Institut D'Electronique Fondamentale,
883 Discipline Physique **NNT** (2012) 2012PA112418.

884 79) S. Ktitorov, G. Simin, and V. Sindalovskii: Soviet Physics Solid State **13** (1972) 1872.

885 80) S. Saito, K. Torii, M. Hiratani, and T. Onai: IEEE Electron Device Lett. **23** (2002) 348.

886 81) A. F. Ho, M. A. Cazalilla, and T. Giamarchi: Phys. Rev. A **79** (2009) 033620.

887 82) T. Matsubara and H. Matsuda: Prog. Theor. Phys. **16** (1956) 569.

888 83) A. Auerbach: *Interacting Electrons and Quantum Magnetism* (Springer, 1994).

889 84) S. Saito, K. Torii, Y. Shimamoto, O. Tonomura, D. Hisamoto, and T. Onai: J. Appl. Phys.
890 **98** (2005) 113706.

891 85) I. B. Spielman, J. P. Eisenstein, L. N. Pfeiffer, and K. W. West: Phys. Rev. Lett. **84** (2000).

892 86) B. Alén, J. Marínez-Pastor, A. García-Cristobal, L. González, and J. M. Marcía: Appl.
893 Phys. Lett. **78** (2001) 4025.

894 87) Y. Sidor, B. Partoens, F. M. Peeters, T. Ben, A. Ponce, D. L. Sales, S. I. Molina, D. Fuster,
895 L. González, and Y. González: Phys. Rev. B **75** (2007) 125120.

896 88) E. Abrahams, P. W. Anderson, D. C. Licciardello, and T. V. Ramakrishnan: Phys. Rev.
897 Lett. **42** (1979) 673.

898 89) A. O. Caldeira and A. J. Leggett: Phys. Rev. Lett. **46** (1981) 211.

899 90) R. A. Stradling and V. V. Zhukov: Proc. Phys. Soc. **87** (1966) 263.

900 91) S. J. A. Jr., D. C. Tsui, and J. V. Dalton: Phys. Rev. Lett. **32** (1974) 107.

901 92) S. G. Engelbrecht, A. J. Reichel, and R. Kersting: J. Appl. Phys. **112** (2012) 123704.

902 93) H. Nishimori and K. Takada: Front. ICT **4** (2017) 2.

903 94) S. Saito, D. Hisamoto, Y. Kimura, N. Sugii, R. Tsuchiya, K. Torii, and S. Kimura: VLSI
904 Technology, Digest of Technical Papers. Symposium on, 2006, pp. 150–151.

905 95) C. A. Doty and D. S. Fisher: Phys. Rev. B **45** (1992) 2167.

906 96) K. J. Runge and G. T. Zimanyi: Phys. Rev. B **49** (1994) 15212.

907 97) D. S. Fisher: Phys. Rev. B **50** (1994) 3799.

908 98) A. Furusaki, M. Sigrist, E. Westerberg, P. A. Lee, K. B. Tanaka, and N. Nagaosa: Phys.
909 Rev. B **52** (1995) 15930.

910 99) S. Saito, K. Torii, Y. Shimamoto, S. Tsujikawa, H. Hamamura, O. Tonomura, T. Mine,
911 D. Hisamoto, T. Onai, J. Yugami, M. Hiratani, and S. Kimura: Appl. Phys. Lett. **84**
912 (2004) 1395.